Modeling 3D Angiogenesis Using Microphysiological System for Preclinical Research

전임상 연구를 위한
삼차원 혈관 신생 체외 모델 개발

February 2021

Graduate School of Engineering
Seoul National University
Bioengineering Major

Somin Lee

전임상 연구를 위한
삼차원 혈관 신생 체외 모델 개발

Modeling 3D Angiogenesis
Using Microphysiological System
for Preclinical Research

지도교수 전 누 리

이 논문을 공학박사 학위논문으로 제출함
2020 년 12 월

서울대학교 대학원
공과대학 협동과정 바이오엔지니어링 전공
이 소 민

이소민의 공학박사 학위논문을 인준함
2021 년 1 월

위 원 장	도 준 상	(인)
부위원장	전 누 리	(인)
위 원	김 성 연	(인)
위 원	신 용 대	(인)
위 원	김 홍 남	

Abstract

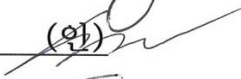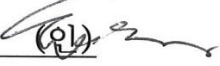Angiogenesis, the formation of new vessel sprouting from the existing vascular network, is essential in vascular maturation during the developmental stage and involves numerous pathologies, including cancer. However, these traditional *in vivo* models used in the field of vascular biology limit the experimental throughput, which is necessary for screening therapeutic targets. Moreover, most *in vitro* models are not physiologically relevant enough to recapitulate complex 3D angiogenesis processes. Therefore, using a microfluidic microphysiological system was suggested as an optimal answer for angiogenesis research. In this thesis, the microphysiological systems recapitulating 3D angiogenesis for preclinical research are introduced.

First, since angiogenesis is a crucial process during the maturation of vascular functionality in the vascular system of the central nervous system (CNS), I designed an *in vitro* blood-brain barrier (BBB) model by mimicking CNS angiogenesis. Compared to the method using vasculogenesis-like network formation, angiogenesis-like vessel sprouting showed more intact interaction with pericyte, which showed a more physiologically relevant BBB structure. Moreover, the functional efflux transport system was recapitulated in the model, which is the primary cause of restricted molecular transport of BBB. Through tri-

culture of all BBB composing cells in the angiogenic sprouting method, p-glycoprotein inhibitor showed more prominent efficacy in the Calcein-AM efflux test than that of endothelial mono-culture condition.

Secondly, the cancer angiogenesis model was designed to test the anti-angiogenic drug efficacy. In specific, siRNA-based regulation of VEGF/VEGFR signaling was tested through the 3D cancer angiogenesis model. In virtue of the model, it was possible to distinguish the effect of the drug between the siRNA targets and among the cancer types, which was difficult to examine in conventional 2D EC assays. Moreover, the model made possible to narrow down the target before the complex xenograft assay, which made the entire preclinical assay process efficient.

In summary, 3D angiogenesis MPS plays an important role in preclinical studies, which provides more relevant and reliable results by reconstituting quantitative 3D angiogenic phenotype. In addition, the throughput of the model and robustness enables more efficient target selection in developing angiogenic-related therapies. Ranging from fundamental studies of pathologies associated with abnormal angiogenesis to the research of novel therapeutic development, the model shows its potential to serve as a robust preclinical model providing an efficient and reliable solution in multiple applications.

Table of Contents

Chapter 3. Modeling Cancer Angiogenesis: 3D Cancer Angiogenesis-on-a-chip for Evaluating the Efficacy of Anti-Angiogenic Drugs 60

List of Figures

vii

Chapter 1. Introduction

1.1. Angiogenesis in Diseases and Cancer

The vascular system plays an important role in vertebrates including human to serve as efficient transport system of nutrients, gas, biomolecules, and cells throughout the organs in complex body. Endothelial cells (ECs), which is the basic building block of the vessel, assembles during the embryonic developmental stage and form tree-like tubular structure to form vascular network, which is called vasculogenesis. In detail, vasculogenesis involves the differentiation, migration and coalescence of endothelial progenitor cells (angioblasts) which is followed by specification to arterial or venous type of vessel in response to complex vascular differentiation molecular signaling including Notch signaling. This continues to the creation of hierarchical system consist of artery, vein, and capillary bed. The complex vascular system is further developed by the sprouting of new capillaries from pre-existing vascular network, a process known as angiogenesis.[1, 2]

Angiogenesis in the later developmental stage accompanies maturation of the specialized function in each organ in response to the biochemical signaling in the local niche. This proves remarkable plastic

capacity of EC to rise diverse organ-specific function, such as barrier properties in blood-brain barrier.[3] However, it also relates with numerous pathologies when the homeostasis of angiogenic activity is disrupted in diverse situations.[4-6] For instance, during the progress of Alzheimer's disease, activated angiogenesis due to brain hypoxia will increase the brain endothelium secreting the neurotoxic peptides which finally kills cortical neurons.[7] Beyond this, abnormal angiogenesis is a major symptom as well as pathological cause in most of ischemic and inflammatory diseases.[4]

Cancer which is the most popular notorious disease in modern human society, is also largely associated with angiogenesis. Cancer angiogenesis is a major hallmark of tumor progression and the most prominent characteristic of the tumor microenvironment (TME). Therefore, regulating cancer angiogenesis has been one of the most promising strategies for cancer treatment.[4, 8-10] Among the molecular pathways involved in pathological angiogenesis, vascular endothelial growth factor (VEGF) and its receptor (VEGFR), has been considered as a major target of regulating cancer angiogenesis.[11] Various anti-angiogenic drugs for cancer treatment, such as the anti-VEGF monoclonal antibody bevacizumab (Avastin), have been clinically

approved and are widely used.[12-14] Although immunotherapy is being newly suggested as a next generation in cancer therapeutics, anti-angiogenic drugs are still the most widely used curing method in the clinics. Moreover, anti-angiogenic drugs are the main focus to be used in combinational therapies to maximize the treatment effect on cancer.[15]

1.2. Traditional Models to Study Angiogenesis

Due to the importance of angiogenesis in human physiologies and pathologies, a number of models and assays were developed and widely used among vascular biologists and researchers studying angiogenesis-related treatments. However, angiogenesis is a complex multistep progress and is affected by various components in surrounding microenvironment the previous models are not sufficient to mimic the entire process of angiogenesis. Moreover, the heterogeneity of ECs depending on organs also correlates with different characteristics in organ-specific angiogenesis. Therefore, it is crucial for the researches to fully understand the potential and features of the angiogenesis assay and determine if it is appropriate for their specific application.

As described in review article collaboratively written by numerous authors in the field of vascular biology[16] (Nowak-Sliwinska et al.,

Consensus guidelines for the use and interpretation of angiogenesis assays, Angiogenesis 2018, 21, 245-532.), a number of *in vivo*, *ex vivo*, and *in vitro* assays are available for angiogenesis studies. One of the popular *in vivo* model of angiogenesis is the mouse dorsal window chamber model, first introduced in 1940s, to directly visualize angiogenesis and microvasculature through window fold tissue at the dorsal skin in live.[17] Another extensively used assay in the field of developmental angiogenesis is whole mount of the mouse retina model. For mouse retina, vessel development continues after the birth so that the retinal plexus grows radially during the first postnatal week. Subsequently, the superficial capillaries begin to sprout at the margin of peripheral retinal. Tip/stalk behavior of ECs during angiogenesis could be observed as well as network remodeling, vessel pruning, lumen formation could be also visualized in each step. Genetically modified mouse could be introduced to identify the role of targeted gene in angiogenesis using this assay. The mouse is sacrificed in the period which correlates to the vascular developmental stage of interest and the retina flat is observed through microscopy.[18] These *in vivo* models reflects the complex process of angiogenesis during the developmental stage, however it has critical limitations in throughput. Since

angiogenesis is a potential target of therapy in numerous diseases including cancer, still a number of drug candidates are waiting to be tested. The importance of the high-throughput for research in anti-angiogenic therapeutics could not be fulfilled in these traditional *in vivo* models. Moreover, as most of *in vivo* models including retinal flat mount and hind limb ischemia model enables the examination of the sprouting at the end point of the experiment, it could not give an assess to the whole process of dynamic angiogenesis. Also, ethical issues and cost and time efficiency could be mentioned as limitations of these model.

On the other hand, *in vitro* models based on human ECs are also widely used in the field of vascular biology. For example, as chemotactic migration of EC is one of the important properties of angiogenesis, would healing assay to examine the migratory potential of ECs in diverse treatment condition is also used as simple and easy assay.[19] However, EC migration assays are not sufficient to represent 3D process of angiogenesis with tip/stalk characteristics of ECs. Therefore, bead sprouting assay was developed to represent 3D angiogenic sprouting *in vitro*. The bead coated with ECs is embedded on fibrin matrix and the 3D lumenized sprouting could be observed in 2-4 days. This assay could be applied with drug or angiogenic factor treatment, as well as could be

tested with genetically modified ECs. This is very simple and physiologically relevant model compared to other *in vitro* assays with EC. However, the model shows a limitation on applying perfusion on the vessel and it is also hard to quantify the sprout due to low uniformity of the sprouting from the bead.

1.3. Microphyiological System for Angiogenesis Study

The microphysiological system including microfluidic organ-on-a-chip platform has emerged in the last decade to great expectations from the pharmaceutical industry. Among all types of tissues or organs as a target of MPS modeling, the vascular system is dominant focus of tissue modeling. The co-culture context and necessity of the gradient generation of biochemical molecules makes vasculature modeling benefit most from microfluidics.[20, 21] Moreover, MPSs of cancers and other organs were also adopting vascular component, referred as vascularization, to enhance the functionality of modeled organ system.[20]

Modeling angiogenesis is more complex progress compared to generating vasculature *in vitro*. Directional chemotactic 3D sprouting of angiogenesis can be only recapitulated *in vitro* through the microfluidic system. This is why there are not many groups working with microfluidic

angiogenic sprout models compared to a number of cases reported with vascular network models. There are two main reasons why microfluidic system is suitable for reconstituting 3D angiogenic sprouting *in vitro*.

First, the microfluidic system is eligible for applying controllable flow in 3D microenvironment. Since the angiogenesis is studied to be highly affected by the interstitial flow or luminal flow, generation of appropriate flow could recapitulate mechanotransductive stimuli in angiogenesis process. The importance of interstitial flow in pathological angiogenesis could be further studied by modeling the angiogenesis through microfluidic platform. For instance, our group has previously reported the angiogenic sprouting model with controllable and directional interstitial flow, which showed that the direction of the stimuli has affected the sprouting direction and speed in the system.[22]

Secondly, 3D cell culture system of microfluidic platform enables recapitulating interactions between ECs and perivascular cells. As fibroblasts were essential for generating 3D lumen of *in vitro* vasculature[23], the 3D microfluidic cell culture system enabled co-culture of ECs with fibroblasts in compartmentalized channels which can generate the gradient of pro-angiogenic factors secreted from fibroblasts crucial for directional sprouting. Moreover, as organ-specific cells such

as pericytes and satellite cells contributes to generating organotypic characteristics of vasculature during the angiogenic progress[3], the 3D MPS system enabled reconstituting organ-specific microvasculature. In addition, as the system is eligible for patterning multiple types of cells in user-designed way, it enables dissecting the role of each cells on angiogenesis which is difficult to clarify in complex *in vivo* system.

For these strength and appropriate characteristics of microfluidic MPS for modeling 3D angiogenesis, our group pioneered the model of angiogenesis which was first reported in 2013.[24] Based on the initial version of model, diverse organotypic angiogenesis models for disease studies could be developed and further applied to testing multiple therapeutic strategies, in collaboration with basic science, clinics, or pharmaceutical industries.
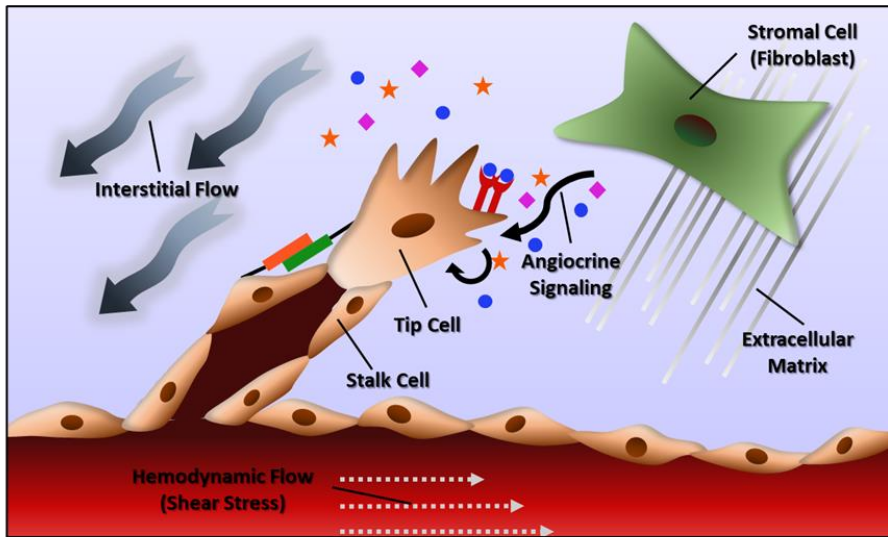
Figure 1.1. Key components within cellular microenvironment regulating angiogenesis. Angiogenesis has been a crucial issue in vascular development or in pathology. Multiple factors are orchestrated to govern this event such as biochemical factors secreted from stromal cells as paracrine signaling or autocrine signaling related to tip-stalk cell biology. Moreover, interstitial flow or shear stress is being regarded as an important biomechanical stimulus for vessel homeostasis.

1.4. Purpose of research

In previous chapters, the importance of modeling angiogenesis for therapeutic studies and traditional angiogenesis models were introduced with their limitations. In this thesis, MPS recapitulating angiogenesis designed for studying organotypic angiogenesis and cancer angiogenesis are introduced. These models were developed and further applied for testing the therapeutic reagents targeting each pathology.

In chapter 2, angiogenesis of central nervous system was recapitulated for modeling blood-brain barrier (BBB). As the development and maturation of barrier function in BBB is previously studied to correlated with signaling of CNS angiogenesis, I approached novel strategy to mimic CNS angiogenesis for developing functionalized model of BBB. One of the functional assays with the developed model, I tested the function of efflux transport system which mainly contributes to barrier system of the BBB. Through applying Calcein-AM assay on the platform, I could verify the effect of efflux transport inhibitors in our system. This result shows the potential of the platform to further apply the model on testing multiple therapeutic strategies regulating this transport system.

In chapter 3, cancer angiogenesis is modeled to study anti-angiogenic drugs. In specific, this project was conducted with a research groups in

chemical department of Seoul National University expertise in nanodrug delivery system and tissue clearing technology, respectively. Our major goal was to develop efficient and robust strategy to evaluate the efficacy of anti-angiogenic nanomedicine, siVEGF or siVEGFR delivered by mesoporous nanoparticle. Multiple assays ranging from wound healing assay to *in vivo* whole tumor vasculature imaging analysis, I could efficiently narrow down the target of the nanomedicine with deep analysis on vasculature. For applying microfluidic cancer angiogenesis assay in this project, I was able to specify the target cancer for the effective nanomedicine treatment before conducting the xenograft model with low throughput. Meanwhile, the MPS model of cancer angiogenesis enabled 3D phenotypic analysis on cancer angiogenic sprouting which was impossible in wound healing assay.

These two representative studies on angiogenesis using the 3D microfluidic MPS, proves the potential of the model to be further applied in disease-specific modeling of angiogenesis and accurate and efficient screening of therapeutic strategies.

Chapter 2. Modeling Organotypic Angiogenesis:

CNS Angiogenesis Model to Reconstitute

Functional Human Blood-Brain Barrier

2.1. Introduction

Blood vessels in the brain cooperate with neuronal and perivascular cells to develop a highly specific microenvironmental niche called the neurovascular unit. The endothelium within the neurovascular unit forms the blood–brain barrier (BBB), which exhibits stronger and more selective barrier function than that of other tissues. The barrier function of the BBB is important to maintaining homeostasis in the central nervous system (CNS) and protects it from pathogens, however, it also blocks numerous drug molecules that may useful for treating CNS diseases.[25, 26]

Specifically, highly developed junction proteins between endothelial cells (ECs) physically restrict hydrophilic compounds, such as polar drugs, from entering the CNS while allowing the passage of essential hydrophobic molecules including oxygen and hormones.[27] The transport of small hydrophilic molecules or potentially harmful materials is tightly

regulated by specific transport systems on luminal and abluminal membranes of brain ECs in an ATP-mediated manner.[28] Importantly, these unique BBB functionalities are acquired via complex cellular interactions during developmental angiogenesis of the CNS.[29-31] Although some molecular mechanisms involved in BBB phenotypes have been discovered, the complex interplay between BBB cell types has yet to be fully elucidated. Thus, much effort has been devoted to developing *in vitro* models to mimic BBB physiology since many genes of interest related to BBB have shown embryonic lethality on *in vivo* models.[29]

As cellular interactions among brain ECs, astrocytes, and pericytes in the BBB microenvironment are critical to developing the BBB phenotype, *in vitro* models have emphasized the importance of co-culture. Static models using a transwell culture system were first introduced in the 2000s; these studies focused on measuring transendothelial electrical resistance (TEER) to determine how pericytes and astrocytes contribute to junction development and barrier integrity. Although early transwell models used mouse brain ECs[32, 33], Hatherell et al.[34] developed a tri-culture transwell model using immortalized human ECs, pericytes, and astrocytes. The strength of these models was the

simplicity in their culture method. However, they could not recreate the dynamic fluid conditions of the CNS vascular niche or the complex physiological anatomy of the BBB.

Recently, microfluidics-based models have made progress towards developing *in vitro* BBB models by providing surmounting these limitations. Ross et al.[35] presented the first microfluidic BBB model having a monolayer of mouse ECs co-cultured with astrocyte which was able to measure TEER in presence of fluidic shear stress on endothelium. A number of studies inspired by this model have employed microfluidic BBB models to study BBB functionality and drug delivery.[36-40] These models demonstrated poor physiological resemblance to the human BBB due to absence of human primary cells, and failed to accurately represent the 3D structure of the luminal vasculature within the surrounding 3D extracellular matrix (ECM) microenvironment.

Within the past couple of years, several 3D BBB vascular models have appeared. Cho et al.[41] designed a 3D BBB model to study neurovascular pathology by introducing neutrophil which extravasates from the 3D rat EC lumen in the presence of a tumor necrosis factor-alpha (TNF-α) chemotactic gradient. Herland et al.[42] used human primary brain ECs, astrocytes, and pericytes in a 3D model to show direct interactions

among cells in the absence of any artificial barrier such as a porous membrane. *In vitro* models of the neurovascular unit consisting of 3D vasculature with neurons and astrocytes have also been introduced and contributed to the establishment of a co-culture protocol for ECs and neuronal cells.[43-45] Campisi et al. developed BBB model having 3D self-assembled vascular network by using iPSC-ECs.[46] However, most of these previous models overlooked the developmental progress of BBB which involves angiogenic process of CNS vasculature development.

Exceptionally, CNS vasculature is not developed via vasculogenesis which is canonical mechanism for common vasculature development. Rather than vasculogenesis, angiogenesis is the main mechanism for development of CNS vasculature in which ECs sprout from the perineural vascular plexus to invade the embryonic neuroectoderm towards a gradient of a proangiogenic factor such as vascular endothelial growth factor (VEGF-A).[29, 47] Several review articles have explained that BBB development occurs in three sequential steps: angiogenesis, differentiation, and maturation.[26, 29, 47] EC phenotypes change in each phase; for example, transcytotic vesicles and leukocyte adhesions are robust in the early angiogenesis phase and decrease during the maturation phase. In contrast, the expression of tight junctions and efflux

transporters is increased between the differentiation and maturation phases, and some CNS angiogenesis-specific molecular systems, such as Glut-1, are regulated by Wnt-β-catenin signaling, which is related to barrier-specific properties.[26, 48] Moreover, Umans et al. also reported that barriergenesis of BBB occurs simultaneously with CNS angiogenesis *in vivo* using zebrafish mutant model.[31] These examples clearly show the strong interconnection between the maturation of BBB functionality and CNS angiogenesis.

I have established a microfluidic-based *in vitro* model by mimicking *in vivo* CNS angiogenesis, thus maximizing the physiological relevance of the model to BBB development. I designed the model to reconstitute the 3D CNS microenvironment, wherein BBB functionality is developed. In this model, all three types of primary human cells (brain ECs, astrocytes, and pericytes) have an *in vivo*-like 3D morphology, with direct cellular interactions occurring within the microfluidic channel. By mimicking the sequential process of BBB development, I was able to confer *in vivo*-like morphology and barrier function on our *in vitro* model. I focused on verifying the efflux transporter system, which is representative of the BBB metabolic barrier mechanism. This functionalized *in vitro* system will potentially serve as a novel platform

to reveal unknown human BBB biology and test the efficiency of drug delivery systems across the human BBB.

2.2. Materials and Methods

2.2.1. Fabrication and designing of BBB-on-a-chip

Microfluidic device was fabricated by polydimethylsiloxane (PDMS, Slygard 184, Dow Corning) using replica molding. The master mold was made through photolithography on silicon wafer using photoresist, SU-8 100 (MicroChem) resulting patterns of microstructure having height of $150 \mu m$. Liquid state of PDMS pre-polymer was completely mixed in 10:1

(w/w) ratio of PDMS base and curing agent, then poured on the master to be polymerized for 30 min on hot plate. PDMS device was gently peeled off from the master, then media reservoirs and hydrogel inlets/outlets were punched using biopsy punch and sharpened hypodermic needle (18 gauge), respectively. Finally, the device was cleaned with adhesive tape to remove dusts or extra PDMS particles, then plasma bonded to be covalently bonded with clean coverslip. As plasma bonding made the device hydrophilic inadequate for patterning hydrogel channels, it was stored on 70 °C dry oven for at least two days before

loading hydrogel in order to restore its hydrophobicity.

2.2.2. Cell culture and chip loading method

Primary human brain microvascular endothelial cells (HBMEC, CellSystems) were cultured in endothelial basal medium-2 (EBM-2, Lonza) supplemented with EGM-2 MV BulletKit (Lonza). Primary human umbilical vein endothelial cells (HUVEC, Lonza) were cultured in EBM-2 supplemented with EGM-2 BulletKit (Lonza). Both ECs were cultured in dish to have less than 80 % of confluency during passaging or experiments. In addition, they are both used in experiments at passage 4 or 5. Primary human pericytes from placenta (hPC-PL, PromoCell) were cultured in pericyte growth medium (PGM, PromoCell) and used in experiments at passage 7 or 8. Primary normal human astrocytes (NHA, Lonza) were cultured in astrocyte growth medium (AGM, Lonza) and used in experiments at passage 6. Primary normal human lung fibroblasts (LF, Lonza) were cultured in fibroblast growth medium (FGM, Lonza) and used in experiments at passage 6. All cells were maintained in culture condition of 5 % CO_2 and 37 °C inside humidified incubator.

For our 3D cell culture of BBB microvasculature, fibrin hydrogel

was basically used for ECM. The fibrin hydrogel solution (10 mg/ml) was prepared by fibrinogen from bovine plasma (Sigma-Aldrich, F8630) diluted in phosphate-buffered saline (PBS, Hyclone), then mixed with aprotinin solution (0.45 U/ml, Sigma-Aldrich, A1153) in volume ratio of 25:4. To generate 3D cellular matrix inside the microchannel, cell suspension is mixed with prepared fibrin hydrogel solution at volume ratio of 3:1 to yield final fibrin concentration being 2.5 mg/ml. The cellular hydrogel solution is injected inside microfluidic channel as soon as it is quickly mixed with thrombin solution (1 U/ml, Sigma-Aldrich, T4648) in volume ratio of 50:1, resulting cross-link of hydrogel around in 3 min.

In order to generate BBB microenvironment for CNS angiogenesis, different types of cells were sequentially loaded inside the microchannel over two days. All of media used in cell culture on microfluidic BBB platform is a mixture of EGM2-MV and AGM in 1:1 ratio, in order to maximize viability and physiological characteristics of both ECs and astrocytes. In first day, LFs were mixed with fibrin hydrogel solution and loaded on the side channel F in final cell concentration of 6×10^6 cells/ml.

Astrocytes followed after being 3D patterned by mixing with fibrin hydrogel solution and loaded on the center channel C in final concentration of 4.5×10^6 cells/ml. After 5 min later while hydrogel was crosslinked enough, media was introduced on top two media reservoirs among four total reservoirs. As the chip is initially hydrophobic during hydrogel loading step, the media could be entirely fill inside the media channels, channel M1 and M2, by vacuum aspiration from other two unfilled media reservoirs. Media was filled enough and samples were incubated at 37 °C overnight. Next day, all media in four reservoirs were aspirated while slight amounts of media remain inside the media channels. The device was tilted in 90° as channel M1 and M2 goes up and down, respectively. Then, 5 $\mu\ell$ of cell suspension, mixture of HBMECs and pericytes in ratio of 6:1 (total cell concentration is 5×10^6 cells/ml), was injected on one of the reservoirs connected to channel M1 in order to make cells to be attached on the left side of previously loaded 3D hydrogel matrix in channel C. The sample was incubated at 37 °C as it was tilted for 30 min which is enough for cells to form focal adhesions on fibrin ECM matrix. Finally, all reservoirs are filled with medium and cultured in humidified

incubator at 37 °C and 5 % CO2.

The sequential cell loading progress described above is one of four co-culture conditions conducted in this research, condition EAP having all composing BBB cells in a 3D microenvironment. For condition E and EP, channel C is filled with acellular fibrin hydrogel (final concentration is 2.5 mg/ml) at the first day. For condition E and EA, cell suspension being introduced to be attached on the side of the central channel C at the second day is only composed by ECs (final concentration is 5×10^6 cells/ml). To avoid the effect of medium component dominating the effect of cellular interactions, culture media are same in all co-culture conditions.

2.2.3. Immumofluoresce assay and analysis on vessel morphology

All samples were fixed with 4 % paraformaldehyde (Biosesang) for 15 min. In advance to introducing antibodies, samples were pre-treated with 0.2 % triton-X 100 (Sigma-Aldrich) during 20 min for permeabilization. Treatment of 3 % bovine serum albumin (BSA, Sigma-Aldrich) followed after for 1 h in order to avoid unspecific bonding of antibodies. All chemical solutions were treated at room temperature and they are introduced inside the microchannel by

adding around 30 $\mu\ell$ on top two reservoirs after aspirating remaining liquid on four media reservoirs. After BSA treatment, the samples were filled with PBS and stored in 4 ℃ before immunostaining.

Antibodies as a marker for specific cell type were introduced after removing PBS. Alexa Flour 488/594/647-conjugated mouse anti-human CD31 (1:200, Biolegend, 303110/303126/303112) was used as EC marker. Alexa Fluor 488-conjugated mouse anti-human GFAP (1:200, BD Bioscience, 560297) was used as astrocyte marker and Alexa Fluor 594-conjugated mouse anti-human α-SMA (1:200, R&D systems, IC1420T) was uses as pericyte marker. They are all treated for 2 days. Hoechst 33342 (1:1000, Invitrogen, C10339) was used for nuclear staining done in an hour. For endothelial junction staining, Alexa Fluor 594-conjucated mouse anti-human ZO-1 (1:200, Life Technologies, 339194), Alexa Fluor 488-conjucated mouse anti-human Claudin5 (1:200, Invitrogen, 352588), Alexa Fluor 594-conjugated mouse anti-human Occludin (1:200, Invitrogen, 331594) and Alexa Fluor 488-conjugted mouse anti-human VE-Cadherin (1:200, eBioscience, 53-1448-42) were used and treated for 2 days. For basement membrane staining,

unconjugated primary antibodies such as rabbit anti-human laminin (1:100, Abcam, ab11575) and rabbit anti-human collagen IV (1:100, Abcam, ab6586) were treated for 2 days, then Alexa Fluor 568 goat anti-rabbit IgG (1:1000, Invitrogen, A11036) was treated as secondary antibody for overnight. All of samples were preserved in 4 °C during immunostaining and maintained in PBS until imaging. For efflux transporter staining, rabbit anti-human P-gp (1:100, Abcam, ab129450), rabbit anti-human BCRP/ABCG2 (1:100, Abcam, ab229193), rabbit anti-human MRP4 (1:50, Abcam, ab233382), and rabbit anti-human GLUT1 (1:100, Abcam, ab115730) were used for 2 days and aforementioned secondary antibody was treated for overnight.

Human Confocal laser scanning unit (Olympus FV1000) with IX81 inverted microscope (Olympus) and Nikon Ti2-E inverted microscope (Nikon Eclipse Ti2) were used to reconstruct 3D microenvironment of BBB network. Images were captured by confocal PMT detector and x10, x20 lenses were used (Olympus). Confocal images were processed by software called IMARIS (Bitplane).

Fiji (http://fiji.sc.), open access software, was used to analyze

confocal images of BBB vasculature. Z-projection of whole stack could result misreading of branch information since two or more vessels will overlap in same position, the sample stacks were divided in lower and upper parts before the projection. After original 3D images were projected and converted into 2D binary masked images, I then conducted measurement of vessel morphology. Total vessel area was calculated in ratio (%) of total vascular area value over total matrix area value ranging from start point of branching. Starting point of branching in each co-culture condition varied so the vessel area was analyzed in ratio of coverage. Average vessel diameter was measured along a line that vertically divides the vessel network into half. All pixel values, 0 or 255 since they were binary images, along the line were measured and we determined the vessel boundary as the value changes to 255. I measured the length of line having continuous value of 255 and recorded as vessel diameter in each sample.

2.2.4. Western blod assay

Expression level of EC adhesion molecule CD31 (PECAM-1) and endothelial tight junction protein ZO-1 were quantified by western blot

assay. PDMS microfluidic chips for the assay were exceptionally attached on PSA film without plasma bonding, instead of cover glass with plasma bonding. This fabrication enabled detachment of chips after culture. After 7 days of culture after EC attachment, samples were washed with PBS for three times. PSA film was removed gently and cellular hydrogel remaining on PDMS piece was lysed in RIPA buffer (T&I) with 1x protease inhibitors. Lysed samples were collected and total protein concentration of each sample was quantified by Bradford assay. 15 μg of protein was separated on SDS-PAGE gel (8 %) and

transferred to PVDF membrane (GE Healthcare). 5 % skim milk in TBS-T buffer (25 mM Tris, 190 mM NaCl and 0.05 % Tween 20, pH 7.5) was used to block PVDF membrane for an hour, then primary antibodies, rabbit anti-ZO-1 antibody (250:1, Abcam), rabbit anti-CD31 antibody (250:1, Abcam) or rabbit anti-β actin (1000:1, Abcam) was applied on each membrane overnight at 4 ℃. Samples were washed again for three times, 30 min each, by TBS-T buffer. IgG-HRP secondary antibody was introduced in concentration of 500:1 or 1000:1 for 1h 30 min at room temperature. Visualization was performed using the Clarity Western ECL substrate (Bio-Rad). Band intensities were measured using Fiji software.

2.2.5. Calcein-AM efflux assay for testing the efficacy of Efflux transport inhibitor

Samples cultured for 9 days after EC attachment were pretreated with p-gp inhibitor Valspodar (PSC-833; Adooq) or p-gp/BCRP inhibitor Elacridar (GF120918; Tocris) in concentration of 10 μM for 10 h. Control groups were also pretreated with DMSO added media at the same time. Then, media of all four reservoirs were removed in each chip and Calcein-AM (ThermoFisher) solution in concentration of 2 μM which includes same initial concentration of inhibitor or DMSO was added on top two reservoirs, 100 $\mu\ell$ individually. After 30 min, solution

was removed and inhibitory media or DMSO control media was filled on reservoirs again for live imaging. The whole center channel of every sample was imaged by confocal microscopy (Nikon Eclipse Ti2) every 0 h, 3 h, 6 h and 10 h right after washing Calcein-AM. All confocal images of each time point were converted to z-projection images. In each sample, fixed position of five ROIs were designated on microvessels and all ROI had same area of square. Mean intensity of designated ROI was measured in each time point and recorded to be analyzed. Initial mean intensity was compared between culture conditions or inhibitor treatment conditions after normalizing each value over the value of non-treated E

only culture condition. Remaining portion of intensity over 10 h ($I_{t=0h}$ / $I_{t=0h}$) was calculated after normalizing every value by initial mean intensity of each condition as 100 %.

2.2.6. Fibrin-HA ECM matrix preparation

Hyaluronic acid (HA) was prepared by HyStemTM Cell Culture Scaffold Kit (Sigma) which consist of HyStem and Extralink1 and they were both prepared in concentration of 10mg/ml. HA and crosslinker was mixed in volume ratio of 4:1. Then the mixture was finally added on prepared fibrin hydrogel solution with cell suspension right before loading in the microfluidic channel. Final concentration of fibrin was fixed as 2.5mg/ml, on the other hand, HA's final concentration was controlled as 0mg/ml, 1.5mg/ml and 2.5mg/ml in each condition.

2.3. Results and Discussion

2.3.1. Microfluidic 3D CNS angiogenesis model reconstituting the BBB microenvironment

To reconstitute the human BBB system, I used our previously developed microfluidic platform [49] which has four channels

compartmentalized by arrays of micro-posts (Figure 2.1). Briefly, channel C is the main region of interest, wherein the 3D BBB microenvironment is developed. Channel M1 and M2 are positioned next to channel C and connected to reservoirs for media supply. Channel F is positioned next to channel M2 to pattern the fibrin hydrogel-embedded 3D stromal cell culture. Channels C and F were filled with human astrocytes and human normal LFs, respectively, and stabilized in 3D fibrin hydrogel for 1 day. HBMECs were then mixed with human pericytes and attached along the M1-C boundary (Figure 2.1). Brain ECs exhibited sprouting from the left side to the right side of channel C, and pro-angiogenic factor gradients were generated by LFs in channel F. Interestingly, pericytes and astrocytes exhibited physical associations with 3D brain microvessels while they sprout toward another side of the channel. After 6 days of culture, ECs reached the other side of the channel and the blood vessel network was perfused (Figure 2.2). I confirmed the perfusion and integrity of the vascular network with FITC-dextran (70 kDa). Most parts of the network were perfused regardless of vessel diameter or density, making the platform eligible for various types of transluminal assays.

Importantly, pericyte coverage was observed along microvessel surfaces,
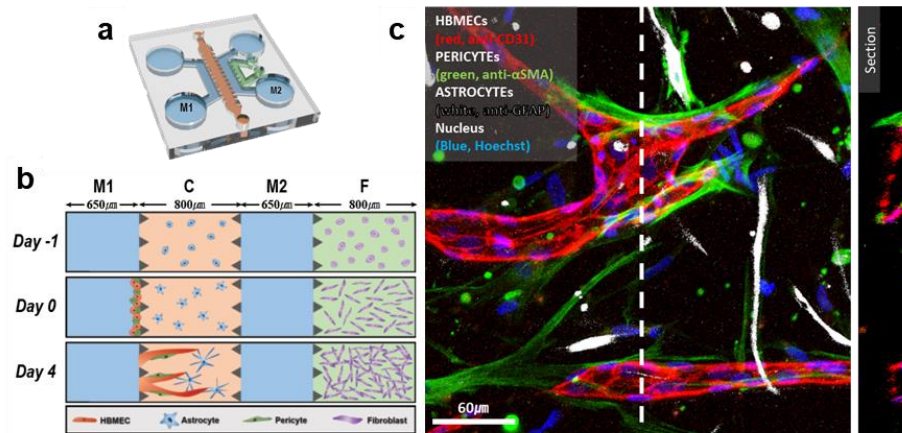
Figure 2.1. Design and cell culture configurations of microfluidic platform mimicking CNS angiogenesis. (a) Schematic view of microfluidic device having three types of microfluidic channel. (b) Section view of microfluidic device describing sequential loading and culture progress of BBB. Channel C (red) is the region where final BBB microenvironment is constructed. Channel F (green) possess 3D fibroblast which acts as source of angiogenic factors. Channel M1 and M2 (blue) are media channel. (c) Confocal imagining at day 6 in higher magnification. Right image is the section view of white dotted line in left image, describing that the vessels are lumenized in 3D. Scale bar: 60 μm.
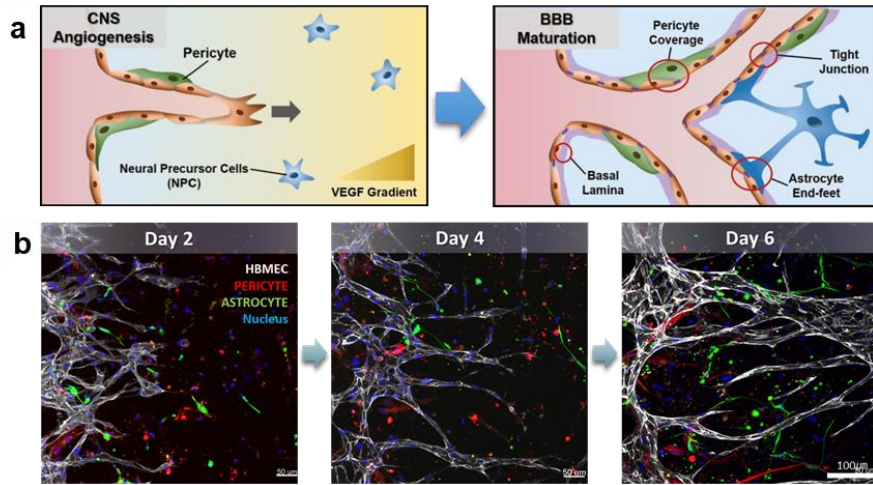
Figure 2.2. Sequential steps of sequential angiogenic sprouting mimicking BBB development. (a) Biological concept of the model to reconstruct 3D *in vitro* BBB by mimicking CNS angiogenesis which sequentially maturated the BBB phenotypes. (b) Day by day confocal imaging of channel C where HBMEC (anti-CD31, red) sprouts from left end to right end. Astrocytes (anti-GFAP, white) protrude to generate end-feet and pericytes (anti-αSMA, green) wrap around EC as day goes by. Nucleus were stained by Hoechst 33342 (blue). Scale bar: 100 *μm*.

whereas multiple astrocyte end-feet directly contacted the perfused network, resembling the constitution of the BBB microenvironment (Figure 2.1). In order to verify how angiogenic mechanism contributes to morphological reconstitution of CNS vasculature, I conducted vasculogenesis-like assay (as previously described in study of Kim et al.[49]) to generate vascular network while co-culturing with same ratio of pericytes and astrocytes used in angiogenesis-based assay. Between two different methods of reconstituting CNS vasculature, I observed prominent difference in perivascular coverage along the microvessels. I could qualitatively visualize that pericytes were aligned more parallel to the microvessels in angiogenesis-based protocol rather than vasculogenesis-like protocol which showed random alignment of pericytes (Figure 2.3). Direct contact and wrapping of pericytes on surface of vasculature was frequently observed through each z-section image of confocal microscopic analysis.

Since *in vivo* BBB vasculature is distinctively developed through angiogenesis, and its functional phenotypes are emerged during the maturation process [29, 47] (Figure 2.2), our main strategy for attaining an *in vivo*-like model was to mimic the CNS angiogenesis. Our microfluidic model allowed long-term culture (> 1 week), and the vasculature had
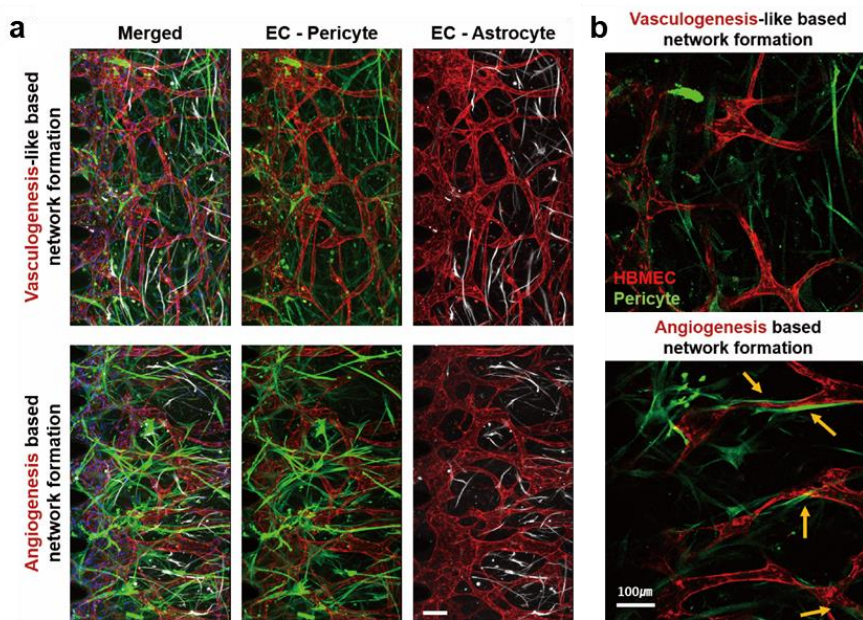
Figure 2.3. Comparison between different 3D vasculature formation assays co-cultured with same ratio of perivascular cells. (a) Representative confocal z-projection images of tri-culture model at day 8 in different protocol of vascular network formation. All three horizontally aligned images for each culture condition is the same ROI. (b) Single projection of confocal microscopic image in higher magnification taken in FigureS2a. Yellow arrow indicates coverage of pericytes around microvasculature. For both Figure S2a and S2b, HBMECs, pericytes, astrocytes and nucleus were labeled by anti-CD31(red), anti-αSMA (green), anti-GFAP (white) and Hoechst 33342 (blue), respectively. Scale bar: 100μm.

matured sufficiently to obtain BBB phenotypes. Morphological phenotypes that recapitulate BBB characters, such as limited vessel dilation, astrocyte end-foot and pericyte coverage on the vessels, were observed about a week of culture; these phenotypes were not visible in early stages of culture (Figure 2.2). Moreover, CNS angiogenesis-based method clearly showed increase of the perivascular coverage compare to vasculogenesis-like network formation method (Figure 2.3). A feasible explnation about this result is that cooperative effect of cerebral pericytes with cerebral microvasculature on its functionality and viability [50]. Thus, mimicking the angiogenic process of BBB development in our model allowed the maturation of *in vivo*-like phenotypes to an unprecedented level.

2.3.2. Endothelial-perivascular cell interaction regulating the morphology of vascular network generated by CNS angiogenesis

It is widely acknowledged that interactions between brain ECs, perivascular cells, and their corresponding microenvironments determine the distinct character of the BBB.[28, 51-57] However, these complex interactions have yet to be simulated by current *in vitro* BBB models.

To investigate how co-cultured perivascular cell types interact with blood vessel cells in our system, I first analyzed the morphology of the blood vessel network co-cultured with endothelial astrocytes (EA), endothelial pericytes (EP), or both cell types (EAP) (Figure 2a). Perivascular cells suppressed blood vessel dilation. The total area and branch width of the vessels significantly decreased under co-culture. Interestingly, EA- and EP-suppressive effects were synergetic under tri-culture (EAP).

The ratio of total vessel area to total ECM matrix area in channel C was measured for each sample (Figure 2.4). I selected this analysis protocol instead of analyzing actual area values because the starting points of branches from the left end of channel C differed among co-culture conditions, as illustrated in the masking images of vessel network (Figure 2.4). Condition E resulted in 53.02 % of coverage at day 7, which was the maximum among all conditions. Under condition EA at day 7, some branches were of similar width to those under condition E, but others were much narrower. Vessels were sparsely distributed along the overall network under condition EA, resulting in the second lowest vessel area percentage (39.27 %). Under condition EP, the vascular network covered 46.71 % of the total vessel area at day 7. Under tri-
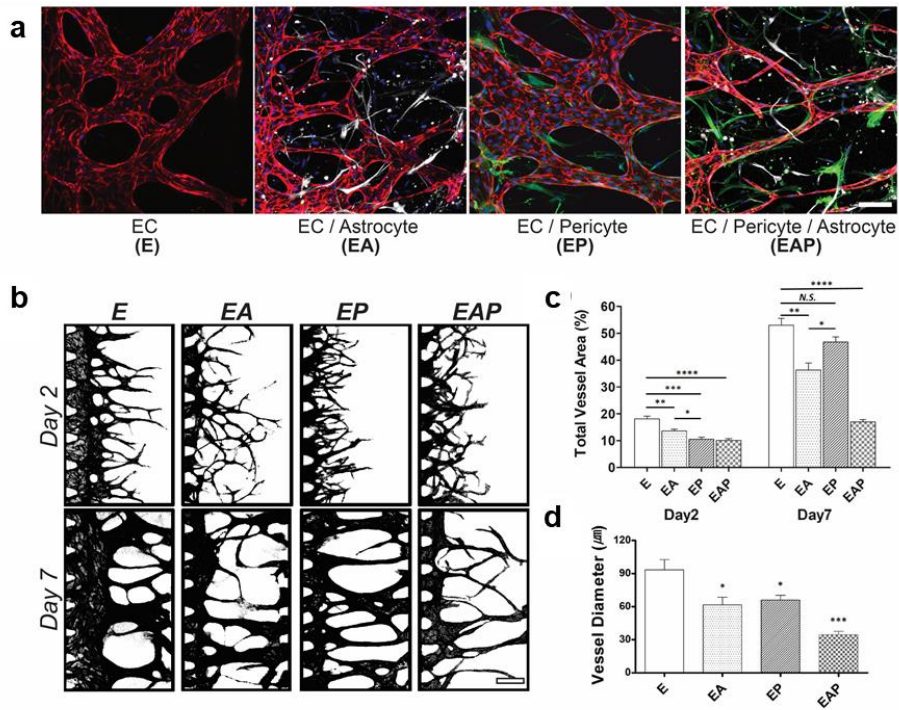
Figure 2.4. Analysis of vascular morphology regulated by different types of perivascular cells. (a) Confocal images of 3D vasculature in each co-culture condition. HBMECs, pericytes, astrocytes and nucleus were labeled by anti-CD31(red), anti-αSMA (green), anti-GFAP (white) and Hoechst 33342 (blue), respectively. Scale bar: 100μm. (b) Masked images of 3D vasculature in each co-culture condition fixed at day2 and day7. Scale bar: 200 μm. (c) Quantitative analysis on total vasculature area at day 2 and day 7 in each co-culture condition. (d) Quantitative analysis on average vessel diameter at day 7 in each co-culture condition. (c, d) N=8 in day 2 condition EA, EP, day 7 condition E, EA and EP; n=10 in day 2 condition E, EP, day 7 condition EAP. Error bars represent SEM. Unpaired two-tailed Student's t-test was performed to obtain statistical comparisons of analyzed values, with the p value threshold for statistical significance set at *p<0.05; **p<0.005; ***p<0.0005; ****p<0.00001.
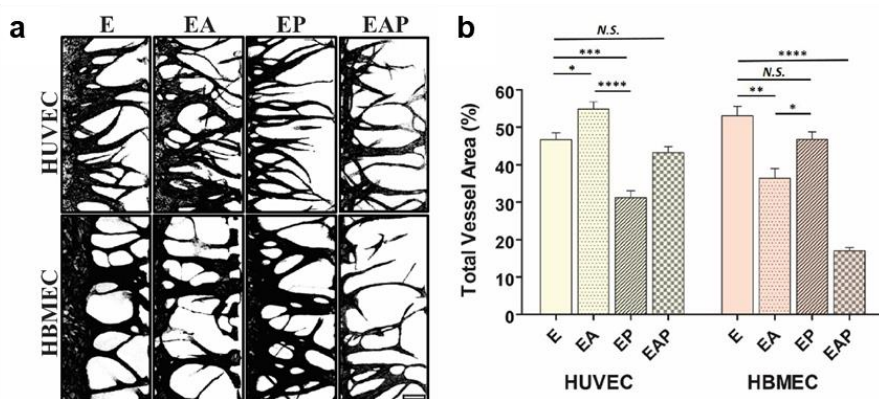
Figure 2.5. Analysis of vascular morphology depending on origin of endothelium. (a) Masked images of 3D vasculature in each co-culture condition using either HUVEC or HBMEC, fixed at day 5 or day 7, respectively. Scale bar: 200μm. (b) Quantitative analysis on total vasculature in each co-culture condition. For HUVEC, n=8 in condition E and EP; n=6 in condition EA; n=12 in condition EAP. For HBMEC, n=8 in condition E, EA and EP; n=10 in condition EAP. Error bars represent SEM. Unpaired two-tailed Student's *t*-test was performed to obtain statistical comparisons of analyzed values, with the *p* value threshold for statistical significance set at *p<0.05; **p<0.005; ***p<0.0005; ****p<0.00001.

culture, the BBB network had significantly lower coverage under condition EAP, at 17.01 %. Differences in vascular geometry among co-culture conditions were not significant during the early stage of CNS angiogenesis, according to the total vessel area at day 2 post-EC loading. This result indicates that morphological characteristics were gained through cellular interactions between ECs and perivascular cells throughout the angiogenic progress. I also examined vessel diameter (Figure 2.4d). The lowest average vessel diameter was observed under condition EAP at day 7, at 34.64 μm, which was 2.7-fold narrower than that under condition E and 1.9-fold narrower than that under conditions EA and EP.

I conducted the same co-culture experiment using HUVEC instead of HBMEC; the origin of these cells does not match the CNS microenvironment. Vessel morphology results for each co-culture condition were very different from those of the HBMEC experiments (Figure 2.5a). I confirmed this finding by quantitative analysis of the total vasculature area at day 5 (Figure 2.5b). Unlike HBMECs, HUVECs under the tri-culture condition did not yield the smallest vascular areas. The largest vessel coverage was observed in the presence of astrocytes and ECs only. These results indicate the importance of the origin of ECs

to the development of *in vitro* BBB models.

I showed critical role of cellular interaction among three cell types constituting BBB in our *in vitro* model (Figure 2.4). BBB vessel is distinctly narrower than other tissue microvasculature.[58, 59] I clearly demonstrated that the diameter of vasculature was narrowest under tri-culture conditions (Figure 2.4d). This trend highlights critical role of endothelia and perivascular cell communication on regulating vascular morphology in our model, although the diameter was slightly larger than known human brain capillaries (8–10μm).[59] As we know, the average diameter of 34.64 μm in this study is the smallest engineered vessel diameter that have been reported hitherto. The origin of ECs also seemed to be responsible for the specific BBB vascular phenotype (Figure 2.5). Using HUVECs originated from umbilical cord failed to represent the characteristic narrow-diameter BBB vasculature. Moreover, co-culture with different types of perivascular cells resulted different tendency compared to that of HBMECs.

2.3.3. Expression of BBB specific junction and basal lamina proteins

A distinguishing phenotypic feature of maturation during BBB

development is the significant expression of junction proteins and basal lamina proteins on ECs. Therefore, I verified these phenotypes in the model by immunofluorescnece and western blot analysis. The expression of endothelial tight junction proteins ZO-1 (Figure 2.7), Claudin-5 (Figure 2.6a), Occuldin (Figure 2.6b) and adherens junction protein VE-cadherin (Figure 2.6a) in HBMECs was individually visualized by confocal microscopy. Occludin showed very low intensity compare to other junctional protiens. Although it showed clear expression in 3D cultured HBMECs, I could not obsesrve junctional expression of Occludin in 2D condition cultured on 96-well plate throguh immunofluorescence analysis (Figure 2.6b).

I was able to clearly confirm differences in expression intensity and geometry due to co-culture conditions, particularly for ZO-1 expression. Four representative images of anti-ZO-1 immunostained (green) HBMECs under different co-culture conditions were taken at the same settings (Figure 2.7). Under condition E (HBEMC mono-culture condition), ZO-1 expression was not significant around cell-to-cell boundary, instead distributed over the cell body. When HBEMCs sprouted in the presence of astrocytes (condition EA), the boundaries between ECs were visible through the ZO-1 junction. However, the
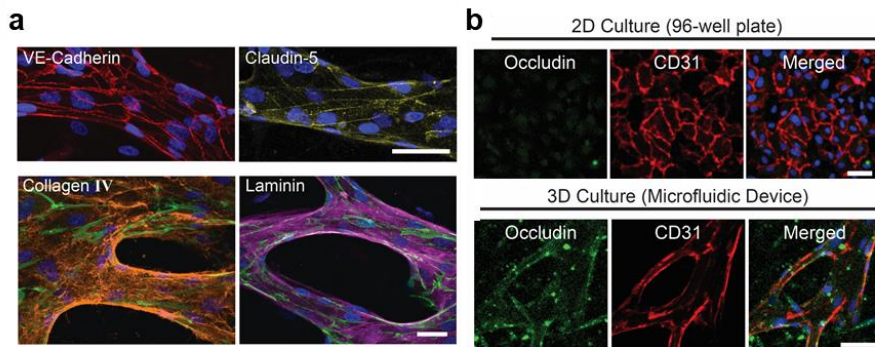
Figure 2.6. Analysis on expression of junction and basal lamina protein in each co-culture condition. (a) 3D confocal image of adherens junction VE-Cadherin (red) and tight junction Claudin-5 (yellow) in tri-cultured vasculature at day 7. Nucleus were labeled by Hoeschst 33342 (blue). Scale bar: 50 μm. 3D confocal image of basal lamina proteins, CollagenIV (orange) and Laminin (purple), in tri-cultured vasculature at day 7. ECs and Nucleus were labeled by anti-CD31 (green) and Hoeschst 33342 (blue), respectively. Scale bar: 30 μm.. (b) 3D confocal image of occludin expression (green) on 3D cultured vasculature and 2D cultured endothelium. CD31(red) is co-stained to clarify the position of vessel. Scale bar: 50 μm.

expression signal was weaker than that under conditions EP and EAP. Condition EAP exhibited the strongest ZO-1 intensity and a clear zipper-like boundary between ECs. These differences in fluorescence intensity indicate that the expression of the ZO-1 tight junction protein was determined by cellular interactions between ECs and surrounding BBB perivascular cells. Moreover, the highest expression level in presence of all types of BBB cells show that BBB maturation was reconstituted in the model.

I confirmed the immunofluorescence result with western blotting (Figure 2.7b). Since the number of ECs in each condition varied (Figure 2.7c), ZO-1 expression level was normalized to the amount of ECs in each sample by CD31 expression level. The ratio of average expression level of ZO-1 over CD31 reached a maximum under condition EAP (2.458) which was 3.36-fold higher than that of condition E (0.731). Ratio of expression level in condition EA (1.162) and condition EP (1.562) was both higher than that of condition E. This quantitative result was consistent with the result of the immunofluorescence intensity analysis. The expression of basal lamina proteins, such as collagen IV and laminin, was then verified in the 3D BBB *in vitro* model. Under condition EAP, vasculature was immunostained after being fully matured
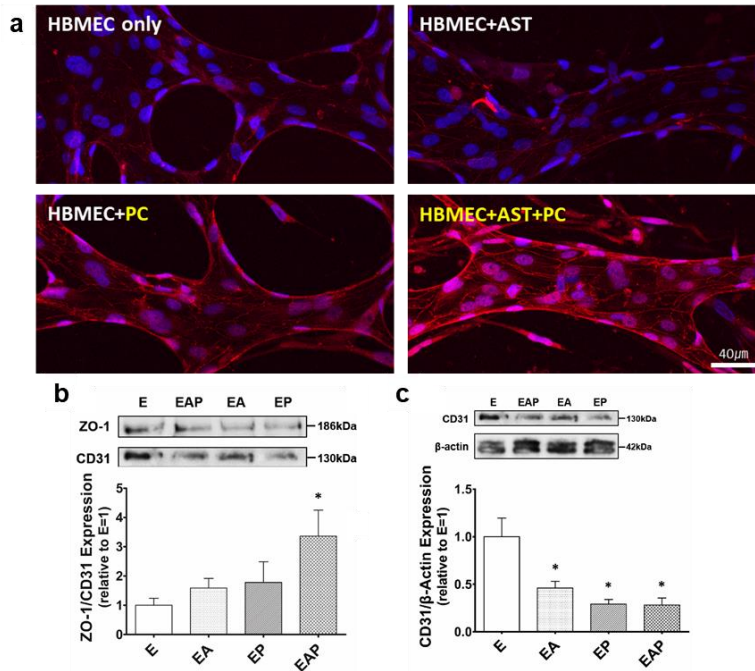
Figure 2.7. Quantitative analysis on expression of junction protein in each co-culture condition. (a) 3D confocal images of ZO-1 tight junction expression at day 7 culture labeled with anti-ZO-1 (green) and Hoechst 33342 (blue). Two representative images were displayed for each co-culture condition. ZO-1 expression on cellular boundary in condition EAP is pointed with yellow arrows. Scale bar: 20 μm. (b) Western blot assay for quantifying ZO-1 expression. Upper image is representative band image of ZO-1 and CD31 for each co-culture condition. Below graph is the result of quantitative analysis on ZO-1 expression level in each co-culture condition normalized against the expression level of CD31. N=6 for condition E, EA and EAP; n=5 for condition EP. Error bars represent SEM. Unpaired two-tailed Student's t-test was performed to obtain statistical comparisons of analyzed values, with the p value threshold for statistical significance set at *$p<0.05$. (c) Western blot assay for quantifying CD31 expression. Upper image is representative band image of CD31 and β-actin for each co-culture condition. Below graph is the result of quantitative analysis on CD31 expression level in each co-culture condition normalized against the expression level of β-actin. N=6 for condition E, EA and EAP; n=5 for condition EP. Error bars represent SEM. Unpaired two-tailed Student's *t*-test was performed to obtain statistical comparisons of analyzed values, with the *p* value threshold for statistical significance set at *$p<0.05$.

for 7 days, and exhibited deposition of basal lamina around the perivascular surface. Confocal images clearly showed a layer of ECM proteins marked with either anti-collagen IV (orange) or anti-laminin (purple), and wrapping ECs marked by anti-CD31 (green) (Figure 2.6a).

Junction expression was also distinguishable in our tri-culture system, unlike in the mono-culture system. I focused on the ZO-1 tight junction for each co-culture condition. Based on immunofluorescence analysis (Figure 2.6) and western blotting analysis (Figure 2.7), tri-culture conditions produced much clear and stronger ZO-1 expression than HBMEC monoculture conditions. All of these aforementioned analyses support the importance of using appropriate cell source and providing comprehensive cellular interactions in order to reconstitute the model which would further applied in drug development or disease studies targeted for human.

2.3.4. Functional efflux transporters eligible for multi-drug resistant assay

Efflux transporters on the surfaces of brain ECs prevent intracellular accumulation of the substrate and exhibit primary BBB barrier function. These transporters restrict the entry of drugs, resulting low success rate
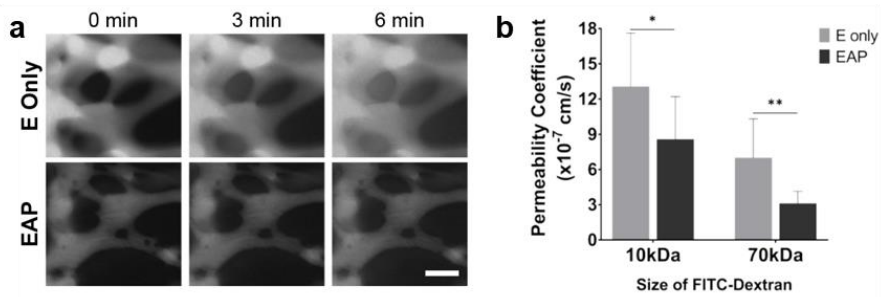
Figure 2.8. Measurement of vascular permeability in 3D BBB vasculature model cultured for 9 days. (a) Representative images of time-lapse fluorescent microscopic imaging of 70kDa FITC-dextran at time 0 min, 3min, and 6min. Scale bar: 200 μm. (b) Quantification of permeability of each culture condition with different size of FITC dextran. N=16 for condition E only and n=13 for condition EAP in assay using 70kDa FITC-Dextran; N=10 for condition E only and n=11 for condition EAP in assay using 10kDa FITC-Dextran. Error bars represent SEM. Unpaired two-tailed Student's t-test was performed to obtain statistical comparisons of analyzed values, with the p value threshold for statistical significance set at *p<0.05 and **p<0.005.

of CNS drug discovery.[57, 60] Among these transporters, p-gp is a well understood ATP-driven efflux pump that is multi-specific to various drugs.[60-62] Therefore, inhibitors of efflux transporters including p-gp were highlighted for use in drug co-treatment, resulting in enhanced effectiveness of the drugs.[60]

Thus, I first checked the expression of four different kinds of BBB-specific efflux transporter molecule (P-gp, BCRP, MRP4, and GLUT1) by immunofluorescence imaging in tri-cultured *in vitro* BBB microvessels. Expression of transporter molecules syncronized with the expression of CD31 which indicates the CNS vasculature in the model (Figure 5a and Figure S5a). Notably, confocal imaging in higher magnification revealed that the p-gp transporter was spatially located in intraluminal side of the ECs (Figure 2.10b, yellow arrowheads in section view).

To demonstrate practical usability of our 3D CNS vasculature system as a CNS drug testing platform, I verified the functionality of efflux transporters under mono- and tri-culture condition. Based on previously described Calcein-AM fluorometric functional assays,[63, 64] I used Ccalcein-AM molecules as a substrate of efflux transporter, especially p-gp and BCRP, to trace the transcellular dynamics of CNS drugs
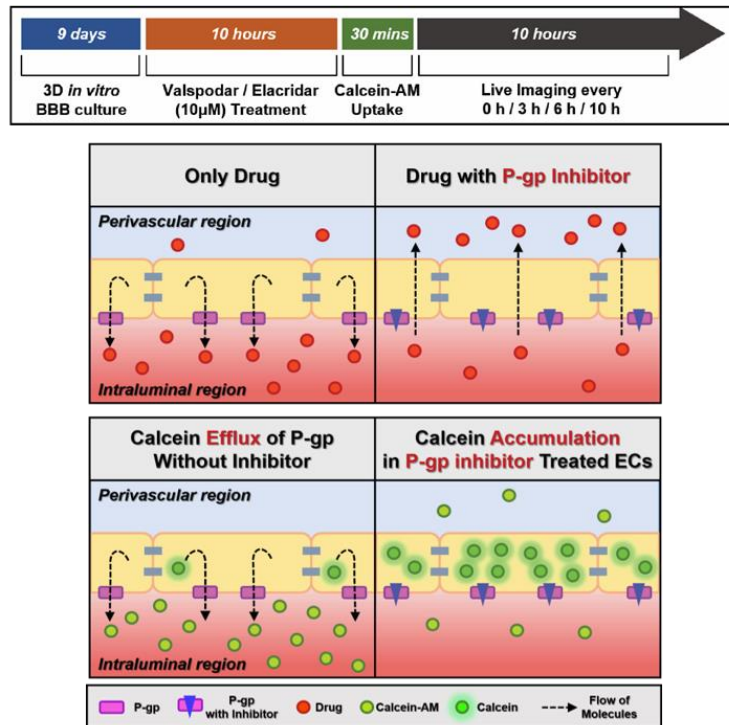
Figure 2.9. Verification of functional efflux transporters in *in vitro* BBB model by testing efflux transport inhibitor via Calcein-AM efflux assay. Schematic description of work flow for Calcein-AM efflux assay in the model. Conceptual description of Calcein-AM efflux assay (bottom) which mimics actual effect of p-gp inhibitor on drug resistance by p-gp *in vivo* (top).
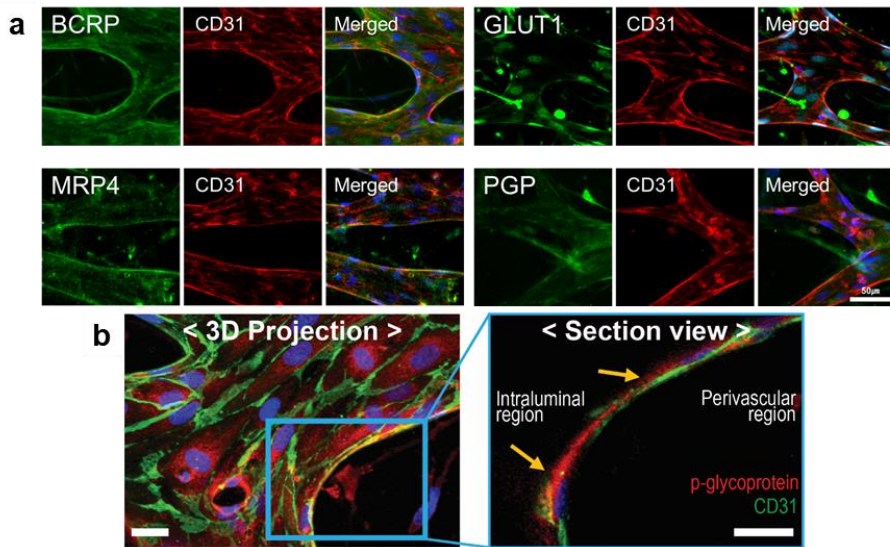
Figure 2.10. Verification of functional efflux transporter expression in *in vitro* BBB model by immunofluorescence staining. (a) Immunofluorescence analysis on expression of p-gp, BCRP, MRP4, and GLUT1 on microvasculature tri-cultured for 8 days. Efflux protein of interest is labeled by anti-pgp or anti-BCRP (green) and HBMEC is labeled by anti-CD31 (red). Scale bar: 50 μm. (b) 3D confocal image of p-gp protein (red) expressed in tri-cultured vasculature at day 7. Right section view is zoomed from left 3D projection image which describes intraluminal oriented expression of p-gp (pointed as yellow arrow heads). ECs and Nucleus were labeled by anti-CD31 (green) and Hoeschst 33342 (blue), respectively. Scale bar: 20 μm.

(Figure 2.9). A fully perfused vascular network of EC monoculture or BBB tri-culture was pre-treated with the p-gp inhibitor Valspodar (PSC-833; Adooq) or p-gp/BCRP inhibitor Elacridar (GF120918; Tocris) for 10 h at a concentration of 10 μM. Calcein-AM (C3100MP; Thermo Fisher) was then introduced at a concentration of 2 μM to be uptaken by ECs for 30 min. Right after washing, the remaining fluorescence of Calcein was monitored at the time point of 0 h, 3 h, 6 h and 10 h using a live imaging system (Figure 2.11). During 10 h of analysis, initial intensity and decrease rate of Calcein fluorescence varied between culture condition or inhibitor treatment condition (Figure 2.11a). Comparison between culture condtition without inhibitor treatment, initial fluorescence intensity was significantly lower in EAP condition than in E only condition. (11.24-fold lower in experimental set testing Valspordar and 5.56-fold lower in experimental set testing Elacridar in Figure 2.11c). The result corresponds to our hypothesis that higher expression of efflux transporters in EAP condition may contributes to higher efflux rate of fluorescence molecules. When I compar the inhibitor treated and non-treated groups, both Valspodar and Elacridar treated group showed significantly higher initial intensity of fluorescence in EAP condition. (For Valspodar in Figure 5f, inhibitor
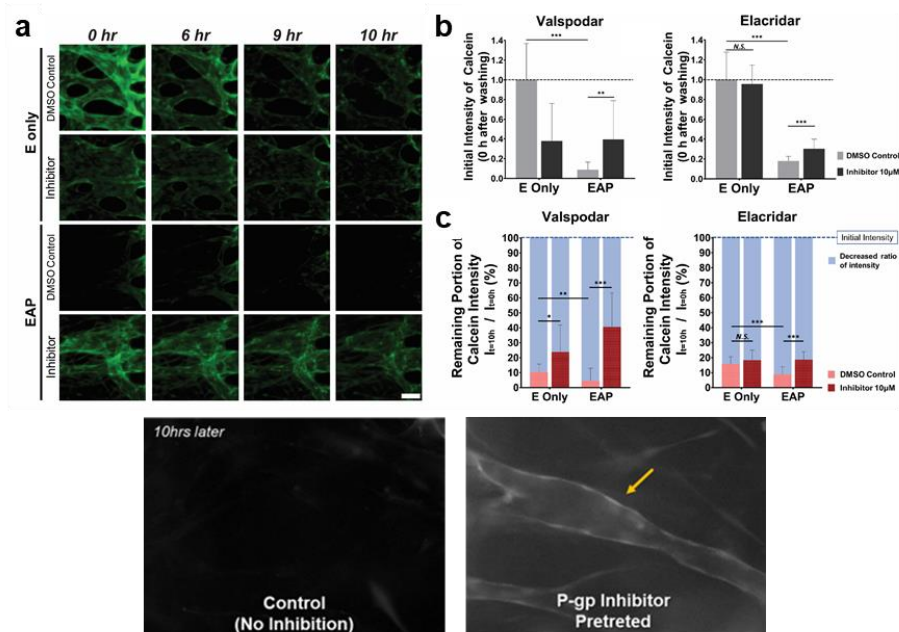
Figure 2.11. Quantitative analysis on the effect of efflux inhibitors in each culture condition. (a) Representative image of Calcein fluorescence in each time point treated or non-treated with 10 μM Valspodar. Scale bar: 100 μm. (b) Initial intensity of Calcein inside intraluminal region of ECs right after washing Calcein-AM solution away was measured in each culture condition and each inhibitor treatment condition. (c) Remaining portion of Calcein intensity inside ECs was calculated as initial intensity was 100 %. For experimental set testing Valspodar in 5f and 5h, n=15 E only/DMSO control; n=16 E only/Inhibitor; n=31 EAP/DMSO control; n=21 EAP/Inhibitor. For experimental set testing Elacridar in 5g and 5i, n=17 E only/DMSO control; n=19 E only/Inhibitor; n=18 EAP/DMSO control; n=18 EAP/Inhibitor. For all graphs from 5f to 5i, error bars represent SEM and unpaired two-tailed Student's t-test was performed to obtain statistical comparisons of analyzed values, with the p value threshold for statistical significance set at *p<0.05; Error bars represent SEM. Unpaired two-tailed Student's t-test was performed to obtain statistical comparisons of analyzed values, with the p value threshold for statistical significance set at *p<0.05 and **p<0.005; ***p<0.0005.

treatment resulted 4.44-fold higher initial intensity than non-treated group; For Elacridar in Figure 5g, inhibitor treatment resulted 1.68-fold higher initial intensity than non-treated group) On the other hand, there was no significant difference in Elacridar treated and non-treated group in E only culture condition.

Since initial intensity of Calcein changed upon inhibitor treatment, I calculated decreased portion of fluorescence from its initial level to compare efflux rate of the moldecules between the groups with different initial Calcein intensity. I measured the percentage of remaining Calcein intensity after 10 h by measuring % of average vascular ROI intensity at 10 h timepoint over 0 h timepoint ($I_{t=0h}$ / $I_{t=0h}$). Remaining portion of Calcein was higher in hinibitor treated groups in both culture condition and in both types of inhibitors. However, EAP culture condition showed more significant difference between treated and non-treated groups rather than E only condition. In EAP culture, Valspodar treatment resulted 8.96-fold higher remaining intensity than non-treated ones (Figure 2.11c) and Elacridar treatment resulted 2.10-fold higher remaining intensity than non-treated ones (Figure 2.11c).

The vascular permeability was also measured in order to verify barrier property of BBB vasculature and to show the potential of our *in vitro* 3D

BBB model in application for further CNS drug transport study. I quantified vascular permeability on E only and EAP culture condition with previously optimized method in microfluidic chip. To ensure FITC-dextran was initially positioned on intraluminal region immediately after introducing to the left media channel, I checked in advance whether the vasculature is fully perfused through the both end of the central channel. Time-lapse fluorescent imaging was conducted every 15 sec starting right after the FITC-solution was introduced to the chip for total 6 min 15 sec (Figure 2.8). By calculating permeability coefficient as described in previous work by Lee et al.[65], I confirmed that tri-culture EAP condition resulted significantly lower permeability compared to E only condition for both 10kDa and 70kDa FITC-dextran (Figure 2.8). For 10kDa FITC-Dextran, the average value of permeability coeffecient was 0.86 x 10^{-6} cm/s for EAP condition (n=11) which was 1.52-fold lower than that of E only condition (n=10) showing 1.31 x 10^{-6} cm/s. For 70kDa FITC-dextran, the average value of permeability coeffecient was 0.31 x 10^{-6} cm/s for EAP condition (n=13) which was 2.29-fold lower than that of E only condition (n=16) showing 0.72 x 10^{-6} cm/s.

Our new 3D *in vitro* BBB system was shown to highly resemble the human BBB in terms of morphological phenotypes; by adopting the

mechanism of CNS angiogenesis, I also attempted to improve platform functionality based on these phenotypes. I first examined the permeability of endothelium generated by CNS angiogenesis in presence of perivascular cells. Since low permeability is a key characteristic of BBB vasculature, a number of previous *in vitro* BBB models have shown permeability measurement of their own. Except the recent model developed by Campisi et al.[46], none of the models have achieved the value of vascular permeability comparable to that of *in vivo*. Although our model showed having higher permeability value than *in vivo*, vascular permeability of our 3D tri-cultured vasculature was lower than majority of previous 3D [40, 42-44] or 2D models.[32, 35] Importantly, the prominent difference in permeability between mono-culture and tri-culture condition in our system indicates that the endothelial-perivascular interaction may contributed to barrier phenotype of BBB vasculature (Figure 2.8).

Metabolic barrier function is another main functional feature that I tried to reconstitute in our 3D system, which was not routinely studied in previous *in vitro* BBB models. It is mainly responsible for preventing CNS drugs from crossing the endothelium into the brain region.[57, 60, 66] By taking advantage of our perfusable vascular network that allowed us

to introduce particles or drugs from intraluminal side, I could flow Calcein-AM molecules through the vessel network, which mimicked the circulation of drug molecules in the blood stream (Figure 2.9). As I tracked the decrease of fluorescence intensity on endothelium over time (Figure 2.11), I could correspond it to efflux rate and compare the value between mono- and tri-culture condition. Initial intensity of Calcein was analyzed in each culture condition and the result showed the lower initial intensity in tri-culture condition compared to that in mono-culture (Figure 2.11). This indicates that the highly functional expression of efflux transport molecules may pumped out the fluorescent molecule during Calcein-AM treatment. For tri-culture condition samples, this effect of efflux transport was diminished in presence in inhibitor, Valspodar (Inhibitor of P-gp) or Elacridar (Inhibitor of BCRP and P-gp), which clarified the function of efflux transporters. At the end, I checked the decrease rate of fluorescence through total time of analysis and concluded that less portion of fluorescent molecule has effluxed if inhibitor was treated (Figure 2.11c). This proves the eligibility of the model as a test platform of CNS drug co-treatment with diverse kinds of efflux transport inhibitors which has been actively studied.[60, 67-69] Several assays and models have been used to study multi-drug-resistant proteins

to modulate barrier function, however, none have attempted to reconstitute the *in vivo* microenvironment of BBB. Although the ultimate goal of regulating this protein is to increase the efficacy of human CNS drug delivery, most tests have been performed in mouse models [67, 70] and some human cell-based platforms have been restricted to 2D culture assays [63, 71, 72] with low physiological relevancy. Recently, a few 3D *in vitro* BBB spheroids having functional efflux transport system were introduced [73, 74] but they lack the structure of 3D perfusable vascular network, which might result limitation on drug application through intraluminal region. Park et al. also represented functional efflux pump on their own developed 2D microfluidic BBB model.[75] This was the first time for *in vitro* BBB model to show regulation of efflux transporters and testing the selective transcytosis of peptides which involve in actual CNS therapeutics. However, majority of previous works have neglected the importance of efflux transport system, thus our model possesses novelty on reconstituting the transport system under 3D condition for the first time. This implicates the potential of the model to be applied on the test of CNS drug penetration in further research.

2.3.5. Matrix modification enhanced astrocyte-endothelium

interaction

The ECM plays a key role in regulating distinct cellular physiology in different tissues. Brain tissue surrounding the BBB is rich in ECM materials such as hyaluronic acid (HA), proteoglycans, and tenascins.[76] The critical role of HA in regulating the astrocyte phenotype *in vitro* has been reported previously.[77-79]

To further recapitulate the distinct star-shaped morphology of astrocytes surrounding blood vessels, I tested the effect of HA in our system. I first loaded astrocytes in the central channel embedded in fibrin 3D hydrogel mixed with different ratio of HA. Next day, I attached HBMEC on the left side of central channel and let them sprout until they reach the right side while interacting with astrocytes and form vascular network in the central channel (Figure 2.12). As the proportion of HA was increased, astrocytes displayed a more star-shape morphology. When fibrin and HA were mixed at a 1:1 ratio (final concentrations of both fibrin and HA were 2.5 mg/mL), astrocytes were more branched than in fibrin gel only. A similar result was obtained when fibrin and HA were mixed at a ratio of 2.5:1.5 (final concentrations of fibrin and HA were 2.5 and 1.5 mg/mL, respectively), and most astrocytes had protrusions. This result agreed well with previous reports.[77-79]
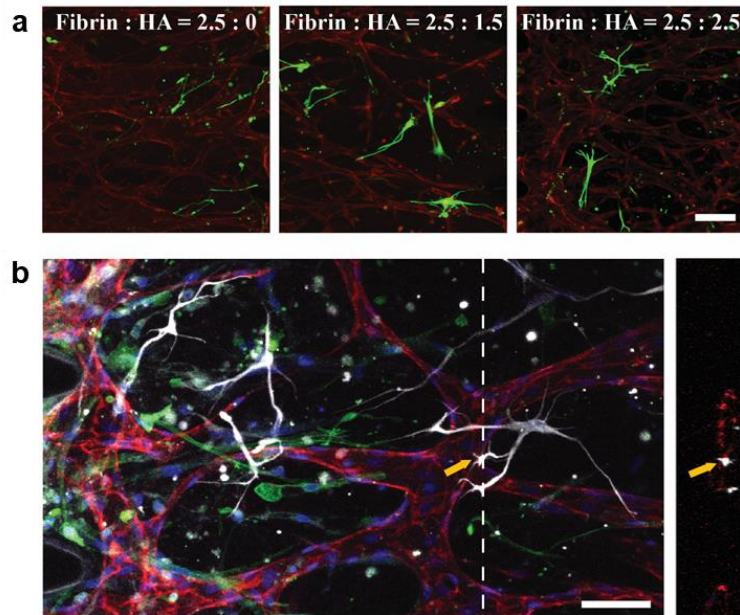
Figure 2.12. Matrix tuning by adding hyaluronic acid (HA) for improvement of astrocyte-EC interaction (a) 3D confocal image of astrocytes (anti-GFAP, green) and HBMECs (anti-CD31, red) in each ECM hydrogel condition having different ratio of fibrin and HA mixture. Scale bar: 100 μm. (b) Representative 3D confocal image of tri-culture of HBMECs (anti-CD31, red), astrocytes (anti-GFAP, white) and pericytes (anti-αSMA, green) in optimally tuned ECM, fibrin and HA mixed in 2.5:1.5 ratio. Nucleus were labeled by Hoeschst 33342 (blue). Right image is the section view of white dotted line in left image, describing direct contact of astrocyte end-feet on vascular surface (yellow arrow head). Scale bar: 70 μm.

Vascular morphology, such as vessel width and lumen structure, was not significantly affected up to the addition of 1.5 mg/mL HA, whereas the effect of HA on astrocyte morphology was saturated at this ratio. Thus, I used a 2.5:1.5 mixture of fibrin and HA to perform a BBB tri-culture assay in the ECM. In the tri-culture model, astrocytes displayed a well-differentiated star-shaped morphology and more protrusions than the line-shaped astrocytes compare to fibrin-only hydrogel. These protrusions projected more astrocyte end-feet on endothelium, which may implicate increased astrocyte–EC interaction in our system (Figure 2.12b).

ECM is another key component governing cell behaviors within the modeled tissues. Brain tissue is composed of complex ECM components, including HA, proteoglycans, and tenascins.[76] Among cells in the human BBB microenvironment, astrocyte phenotype and morphology are known to be largely influenced by the local microenvironment.[77, 79] This was clearly demonstrated by Placone et al.,[78] who manipulated the type and ratio of ECM including HA, and analyzed astrocyte morphology and active states under each ECM condition. To recapitulate the distinct star-shaped astrocyte morphology in the 3D *in vitro* model, I tuned the 3D ECM base using previously developed protocols.[78, 80] Based on these

previous studies on materials, I was able to obtain astrocytes with many protrusions by tuning fibrin hydrogel with HA; this morphology was crucial for enhancing astrocyte–EC interactions, such as outer vessel wall end-foot structures (Figure 2.12b). This is more than simply mimicking morphological structure since numerous studies have reported that astrocyte end-feet enhances the role of astrocytes in controlling homeostasis and repairing vascular damage in the CNS.[28, 51, 81]

2.4. Conclusions

In this study, I reported a novel 3D *in vitro* BBB model which mimicked development of CNS angiogenesis. This strategy relies on biological knowledge that the maturation of BBB barrier phenotypes occurs during process of CNS angiogenesis which is distinct from typical vasculature development of other tissues. In this platform, primary human brain ECs exhibited BBB phenotypes such as narrow vascular morphology, high tight junction expression, low permeability, and a functional metabolic barrier system only when co-cultured with both perivascular cells. In particular, this model allows us to observe penetration of molecules through luminal part of the blood vessel under 3D condition. I believe

this model has strong potential as an assay to study transport characteristics of CNS drugs.[82] Moreover, the model has an advantage to test CNS medications targeting pathological angiogenesis of brain tumor[30] or brain damage[83-85] since the model is based on quantitative anagiogenesis assay. Combining this BBB tissue engineering with the emerging technology of high-throughput screening systems [20, 86] will permit the practical use of this model in pre-clinical tests and translational research, to develop improved CNS medications in the near future.

Chapter 3. Modeling Cancer Angiogenesis:

3D Cancer Angiogenesis-on-a-chip for evaluating

the efficacy of anti-angiogenic drugs

3.1. Introduction

Cancer angiogenesis is a major hallmark of tumor progression and the most prominent characteristic of the tumor microenvironment (TME). Therefore, regulating cancer angiogenesis has been one of the most promising strategies for cancer treatment.[4, 8-10] Among the molecular pathways involved in pathological angiogenesis, vascular endothelial growth factor (VEGF) and its receptor (VEGFR), has been considered as a major target of regulating cancer angiogenesis.[11] Various anti-angiogenic drugs for cancer treatment, such as the anti-VEGF monoclonal antibody bevacizumab (Avastin), have been clinically approved and are widely used.[12-14] However, effective production and minimization of side effects remain susceptible. This spurred considerable effort in recent years to target VEGF signaling.

Among the approaches, RNA interference (RNAi) has immense potential in terms of therapeutics because of its high selectivity and ease

of synthesis.[87-90] Several studies have demonstrated the anti-angiogenic potential of RNAi targeting VEGF pathway in tumors; many of studies were based on small interfering RNA (siRNA) accompanied by a nanocarrier, referred to as nanomedicine.[91-97] However, two-dimensional (2D) *in vitro* models used in the aforementioned RNAi studies were not optimized for analysis of the anti-angiogenic effects because they did not reflect pathological 3D sprouting of endothelial cells (ECs).

Several *in vitro* models of cancer angiogenesis using microfluidic organ-on-a-chip technology have recently been reported.[98-105] By providing the 3D TME with an angiogenic factor gradient and biomechanical stimuli, the microfluidic organ-on-a-chip technique exclusively enabled recapitulation of functional 3D angiogenic sprouting *in vitro*.[22, 24, 106, 107] Despite the advent of physiologically relevant *in vitro* models of 3D angiogenesis, evaluating the effect of nanomedicine specifically designed for anti-cancer angiogenesis still lacks adopting appropriate *in vitro* model to clearly assess targeted phenotype such as inhibition of pathological EC sprouting.

In this chapter, I suggest an efficient strategy for accurate assessment of anti-angiogenic drugs. I aimed to develop and apply a tumor vascular model enabling systematic and reliable analysis on the anti-angiogenic

effect (Figure 3.1). I have conducted this research in collaboration with research groups in chemical department who are specialized in designing nanomedicine and developing novel technique for 3D tissue imaging, respectively. Prior to embarking on an experiment, based on the advantages including nucleic acid delivery efficacy and safety of Mesoporous Silica Nanoparticle (MSN)[108-110], we selected the target for siRNA (siVEGF or siVEGFR) and choose MSN as a representative delivery carrier. We conducted rapid molecular analysis on ECs to verify the result of target gene interference in 2D cultured system. Next, we introduced microfluidic cancer angiogenesis-on-a-chip recapitulating 3D angiogenic sprouts in TME for efficient screening of siVEGF/MSN or siVEGFR/MSN, narrowing down the potential targets and ranges of the anti-angiogenic effect. Finally, 3D vascular mapping of human tumor xenograft using the clear, unobstructed brain imaging cocktails and computational analysis (CUBIC)-based tissue clearing technique was applied for accurate and unbiased imaging on whole tumor tissue vasculature. We considered various parameters for quantitative analysis of tumor vascular morphology, and the analysis was extended to sub-regions of the entire tumor tissue. Our strategy demonstrated the precise and reliable evaluation on anti-angiogenic effect as the changes in 3D

morphological phenotype of vasculature, which was evidenced by our comprehensive and sequential assessment. We anticipate that the robust strategy of the cancer angiogenesis model and 3D imaging-based analysis will provide a fresh perspective for accurate assessment of the efficacy and safety of potential anti-angiogenic nanomedicine.

In addition to the collaborative research to develop strategy for evaluating anti-angiogenic nanomedicine, this chapter also briefly suggests the development of high-throughput platform to robustly assess multiple types of anti-angiogenic drugs. Recent advances in microfluidic organ-on-a-chip technology have enabled the growth of 3D microphysiological systems for diverse biological studies. Fabrication and usage limitations inherent to conventional soft lithographic PDMS-based microfluidic platforms drive demands for more accessible, standardized, and mass producible platforms for wider applications. I introduced a novel injection-molded plastic array 3D culture platform (IMPACT), a microfluidic system designed for easy and diverse patterning of 3D cellular hydrogel. The flexibility of the IMPACT platform enabled simultaneous high-content morphological profiling of angiogenic potential of nine different types of cancer cells. Moreover, screening of three different known anti-angiogenic drugs was done at

various dosages. Distinct and expected molecular mechanism dependent response on both tumor and vasculature in response to treatment was observed, I confirmed the applicability of the platform as high-content drug testing tool. As two different projects shown, this chapter describes modeling 3D cancer angiogenesis could be applied in evaluating anti-angiogenic drugs in more efficient and physiologically accurate manner.
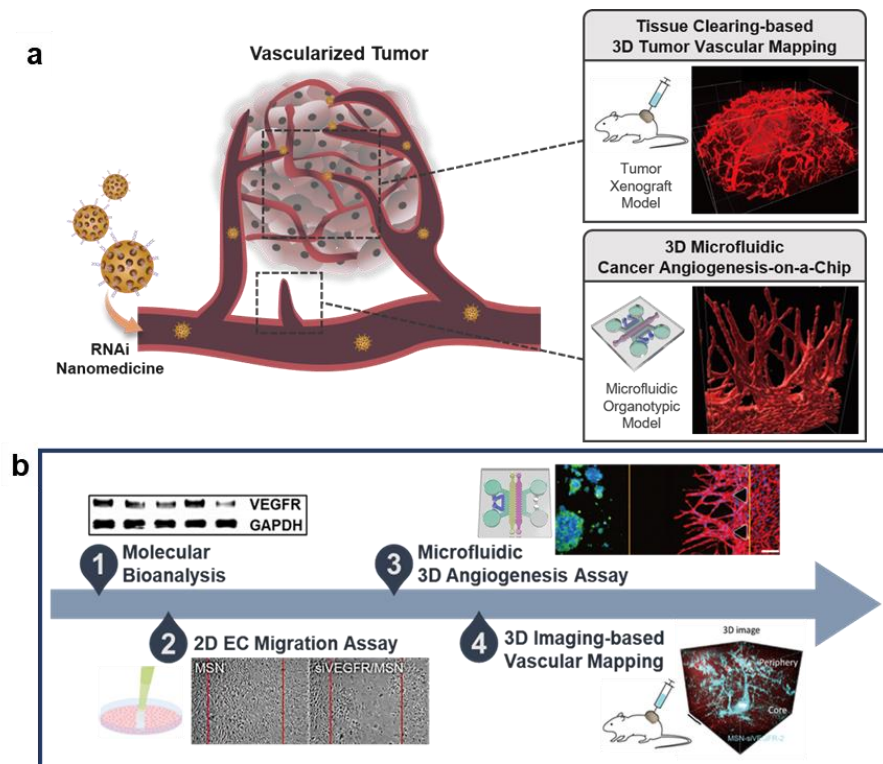
Figure 3.1. Systematic strategy to assess the efficacy of anti-angiogenic nanodrug. (a) Schematic overview of the research on RNAi-based nanomedicine evaluation using 3D microfluidic cancer angiogenesis-on-a-chip and tissue clearing-based 3D tumor vascular mapping technology. (b) Systematic progress of assessment on anti-angiogenic nanomedicine using multiple types of assays.

3.2. Materials and Methods

3.2.1. Fabrication and designing of the PDMS chip

Microfluidic chips were fabricated in polydimethylsiloxane (PDMS, Sylgard 184, Dow Corning) using the method of replica molding. PDMS elastomer and curing agent is mixed in ration of 10:1 (w/w) and poured on master mold having computer aided designed (CAD) microstructure fabricated by photolithography. After few minutes on hot plate, PDMS is crosslinked to be solid but elastomeric, and it is ready to be peeled off from the master. Then, inlets and outlets of the channels were punched with biopsy puncher and finally, PDMS replica is plasma bonded with cover glass to generate strong covalent bond. The height of channels in microfluidic chip is around 100-150 μm. All of fabricated chips were then stored in 70 °C dry oven until cell loading experiment in order to make them hydrophobic for hydrogel patterning.

3.2.2. Cell culture and chip loading method

Human umbilical vein endothelial cells (HUVEC, Lonza, Switzerland) were cultured in endothelial growth medium (EGM-2, Lonza,

Switzerland) with full supplements and used at passage number 4-5. Normal human lung fibroblasts (LF, Lonza, Switzerland) were cultured in fibroblast growth medium (FGM-2, Lonza, Switzerland) with full supplements and used at passage number 6-7. Cells were grown to 80% of confluence in dish prior to passaging or experiments. All of cell lines used in the study, SW620 (human colorectal adenocarcinoma), A549 (human adenocarcinomic alveolar basal epithelial cell), HepG2 (human hepatocellular carcinoma), U-87 MG (human glioblastoma), 786-O (human renal cell epithelial adeonocarcinoma), and MCF7 (human mammary gland epithelial adenocarcinoma), were cultured in RPMI-1640 (Gibco, USA) and DMEM (Welgene, Korea) supplemented with 10% FBS and 1% P/S in 37 °C and 5% CO_2. Right before cell loading in microfluidic device, cells were detached from the culture dish using 0.25% trypsin-EDTA (HyClone, USA) and re-suspended with EGM-2 in certain concentration needed for each experiment.

Two types of 3D microfluidic chips reported in previous works[22, 24] were used for angiogenesis and cancer angiogenesis assay, respectively. For 3D fibrin hydrogel preparation for both assays, bovine fibrinogen (Sigma) was dissolved in PBS (HyClone) having concentration of 10 mg mL^{-1} supplemented with aprotinin (0.15 U mL^{-1}, Sigma). In all cases,

acellular hydrogel patterning was done with fibrin hydrogel in final concentration of 2.5 mg mL^{-1}. On the other hand, cellular hydrogel patterning was done by mixing cell suspension with prepared hydrogel also making final concentration as 2.5 mg mL^{-1}. In angiogenesis assay without cancer, microfluidic chip with a single central channel was used with same loading sequence described in previous work.[24] In brief, fibroblast was initially loaded on side channel and acellular hydrogel was loaded on central channel, then next day, HUVECs were attached onto the one side of central hydrogel channel making ECs to be sprout on central channel toward the fibroblasts. For cancer angiogenesis assay, microfluidic chip having two central channels introduced in previous work[22] was used with modified cell loading protocol.

In this work, cancer alone could not efficiently generate angiogenesis sprout. Therefore, fibroblasts were used in every culture condition for providing of basal level of angiogenic factors. A day before HUVEC attachment, Fibroblasts, cancer cells, acellular fibrin hydrogel were 3D patterned on channel F, T and C, respectively as described in Figure 3.3. HUVECs were attached on the side of central channel by flowing HUVEC suspension on media channel. The chips were tilted by 90 degrees for 30 min for cells to attach evenly on the surface of 3D fibrin

hydrogel. Angiogenic sprouts were generated on central channel toward cancer cells and fibroblasts. The final concentration of fibroblasts and cancer cells were 5×10^6 cells mL^{-1} and 3×10^6 cells mL^{-1}, respectively, when mixed with 3D hydrogel and the volume of HUVEC suspension (5×10^6 cells mL^{-1}) introduced in each chip was 5 μL. Around 0.5 mL of EGM-2 media was applied on four media reservoirs after finishing all hydrogel loading with same height level. A day after EC attachment, EC were stable applied on surface of channel forming 2D monolayer. At that time, media was removed to apply siVEGF/MSN or siVEGFR/MSN into the media channel in siRNA concentration of 100 nM, respectively. Serum-free media with nanoparticle and siRNA complex was exposed to cells loaded inside the chip for 6 h, then the media was replaced with normal media for culture.

After 3-5 days of angiogenesis assay, samples were fixed with 4% paraformaldehyde (Biosesang) for 15 min and permeablization followed after using 0.2% triton-X 100 (Sigma-Aldrich) for 20 min. 3% bovine serum albumin (BSA, Sigma-Aldrich) was treated for 40 min to avoid unspecific bonding before applying antibodies for immunofluorescence. Alex Flour 488-conjugated mouse anti-human cluster of differentiation 31 (anti-CD31, Biolegend) was used as EC marker. Alex Flour 594-

conjugated anti-epithelial cell adhesion molecule (anti-EpCAM; CD326, Biolegend) was used as cancer cell line HepG2 marker. Nuclear stainning was performed using Hoechst 3342 (Invitrogen). All of fluorescence molecules were diluted in BSA and applied on chip for incubation for 2 to 3 days. Imaging was performed using confocal microscopy (Olympus FV1000 and Nikon Eclipse Ti2-E, Japan) to reconstitute 3D imaging of angiogenic sprouts with or without cancer cells.

3.2.3. Preparation of anti-angiogenic nanomedicine mediated by mesoporous nanoparticle delivery

MSN was prepared according to the previously reported methods.[111, 112] The pore size, surface area, and pore volume of the MSN particles were analyzed through nitrogen sorption experiments. Nitrogen adsorption isotherms were obtained by using a NOVA Surface Area Analyzer (Nova 2200e, Quantachrome instrument, USA). Prior to the measurements, the sample was degassed for 12 h at 573 K. The specific surface area was calculated by the Brunauer-Emmett-Teller (BET) equation using the adsorption data obtained in the pressure range $P/P_0 = 0.05 \sim 0.2$, whereas the pore size distribution was analyzed with the

adsorption branch of the nitrogen adsorption isotherm according to the Barrett-Joyner-Halenda (BJH) algorithm. The morphological study was carried out by using transmission electron microscopy (TEM, LIBRA 123, Carl Zeiss) and zeta potential were measured by zetasizer NS90 (Malvern, UK).

Primers and siRNAs and scrambled siRNA for negative control (N.C-siRNA, Cat. SN-1003) were purchased from Bioneer (Korea). The sequence of siRNA targeting VEGFA (siVEGF) were GGAGUACCCUGAUGAGAUC (sense) and GAUCUCAUCAGGGUACUCC (anti-sense).[91, 113, 114] The sequence of siRNA targeting VEGFR2 (siVEGFR) were GGAAAUCUCUUGCAAGCUA (sense) and UAGCUUGCAAGAGAUUUCC (anti-sense).[115-118]

3.2.4. Immunofluorescence assay and 3D image analysis

Fluorescence 3D confocal images from microfluidic angiogenesis assays were analyzed automatically by using Fiji (http://fiji.sc/Fiji) or Imaris software (Bitplane). To quantify vascular volume, 3D angiogenic sprouting was smoothed and the surface was semi-automatically reconstructed using surface tool. For quantification of area, the number

of vascular junctions, and sprout length, 3D images were z-projectioned and maked from the backgrounds in advance using Fiji. Masked images were analyzed with the diverse parameters using Angiotool software.[119]

3.2.5. High-throughput injection-molded plastic array platform for modeling TME

Fabrication of chip: Polystyrene (PS) injection molding was performed at R&D Factory (Korea). The aluminum alloy mold core was processed by machining and polishing. The clamping force at the time of injection was set to 130 ton with a maximum injection pressure of 55 bar, 15 s of cycle time, and a 220 °C nozzle temperature. A PS substrate plate was then subsequently bonded to the upper bulk chip via ultrasonic welding (Branson, USA).

Cell Loading: Prior to device seeding, all chips were plasma surface treated at 70 W for 3 min to induce surface hydrophilicity (Femto Science, Korea). Fluid patterning within the device was done in the following sequence: round channel, center channel, and reservoir floor (if needed). Round channel patterning was done by mixing 50 µL of a cellular or acellular bovine fibrinogen solution (final concentration 2.5 mg/mL; Sigma, USA) with 1 µL of bovine

thrombin (0.5 U/mL; Sigma). Next, 1.5 µL of the cellular or acellular fibrinogen and thrombin mixture was injected along the edge of the outer channel, where the capillary forces spontaneously captured and patterned the droplet along the round channel. The primed hydrogel mixture was then allowed to crosslink for 3 min before the center channel was patterned. The center channel was patterned by mixing 50 µL of a cellular or acellular bovine fibrinogen solution (final concentration 2.5 mg/mL) with 1 µL of bovine thrombin (0.5 U/mL). The cellular or acellular fibrinogen and thrombin mixture was injected into the center channel via the injection port until the entirety of the center channel was filled. The primed hydrogel mixture was then allowed to crosslink for 3 min before the media reservoirs were filled with medium. In the case that the media reservoir floors also needed to be patterned, this was done immediately after the center channel patterning. The media reservoir floor was patterned by mixing 50 µL of a cellular or acellular bovine fibrinogen solution (final concentration 2.5 mg/mL) with 1 µL of bovine thrombin (0.5 U/mL). Next, 10 µL of the cellular or acellular fibrinogen and thrombin mixture were injected onto the reservoir floor and allowed to crosslink for 3 min before

the media reservoir was filled with 200 µL of medium.

3.2.6. Multiple types of anti-cancer treatment

Cetuximab (a gift from Professor Jo at Samsung Hospital) was diluted into three different concentrations (0.01, 0.1, and 1 mg/mL) with EGM-2 and introduced into the media reservoir. For inhibitors, three doses were tested at concentrations of 1, 10, or 100 µM for Fluorouracil (5-FU; a gift from Prof. Jo at Samsung Hospital) and 0.1, 1, and 10 nM for Axitinib (Selleckchem, USA). The inhibitors were dissolved in DMSO according to the manufacturers' instructions and added to the cell culture reservoir.

3.3. Results and Discussion

3.3.1. Regulation of 3D angiogenesis *in vitro* by siVEGFR/MSN in microfluidic chip

To evaluate the effect of siVEGF/MSN or siVEEGFR/MSN on the 3D angiogenic phenotype, we applied microfluidic organ-on-a-chip model. Prior to the study of cancer angiogenesis in different types of tumor, we preliminarily investigated anti-angiogenic effect using previously
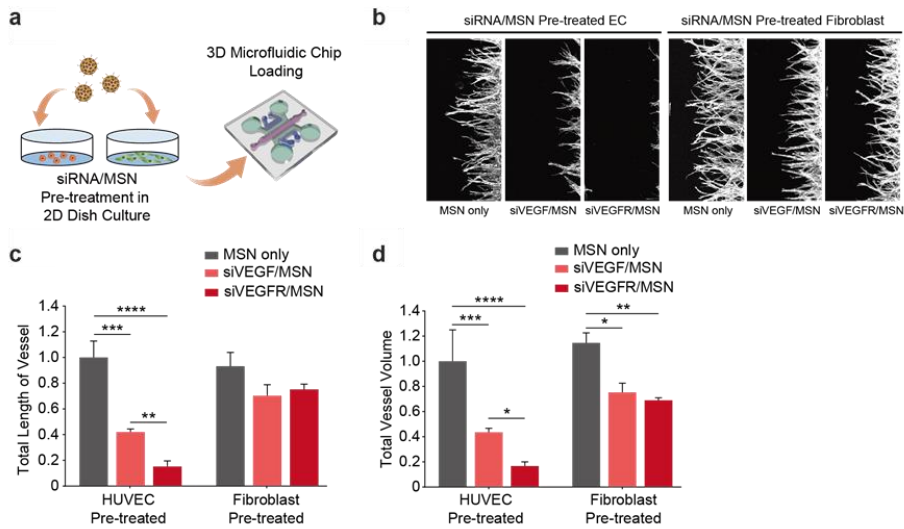
Figure 3.2. 3D microfluidic platform-based in vitro angiogenesis assay using siVEGF/MSN or siVEGFR/MSN pre-treated HUVEC or fibroblast. (a) Schematic overview of experimental progress. (b) Representative z-stacked confocal image of angiogenic sprouts in different treatment condition. Scale bar is 300 μm. (c), (d) Quantitative analysis on total vasculature volume and total vessel length in each treatment condition. (*p < 0.05, **p < 0.01, ***p < 0.001, ****p < 0.0001, Two-way ANOVA with subsequent Turkey's multiple comparisons post-test, n = 3 to 6 for each condition).

developed 3D angiogenesis-on-a-chip model (Figure 3.3).[22, 24] We performrmed two separate microfluidic angiogenesis assays, according to the methods by which siVEGF/MSN or siVEGFR/MSN was applied.

First, we conducted a 3D angiogenesis assay using HUVECs and normal fibroblasts pre-treated with siVEGF/MSN or siVEGFR/MSN, prior to introducing these cells onto the chip. Cells were prepared in 2D dish culture and exposed to MSNs loaded with or without siVEGF or siVEGFR for 6 h. They were then detached from the dish and loaded onto the chip for a 3D angiogenesis assay (Figure 3.2a). The degrees of on-chip 3D angiogenesis differed depending on whether the cells had been pre-treated with siRNA/MSN (siVEGF and siVEGFR) or not (Figure 3.2b). Notably, pre-treated HUVECs (HUVEC pre-treated) showed a more dramatic reduction in angiogenesis after siRNA/MSN treatment, compared to pre-treated fibroblasts (Figure 3.2c and 3.2d). In HUVECs, siVEGFR/MSN pre-treatment resulted in a more prominent anti-angiogenic phenotype, compared with siVEGF/MSN pre-treatment (Figure 3.2c and 3.2d). These results highlight the function of VEGFR as a key regulator of the VEGF/VEGFR molecular pathway; depletion of VEGFR on the cellular membrane of EC blocks series of downstream signaling responsible for angiogenesis.[10, 14]
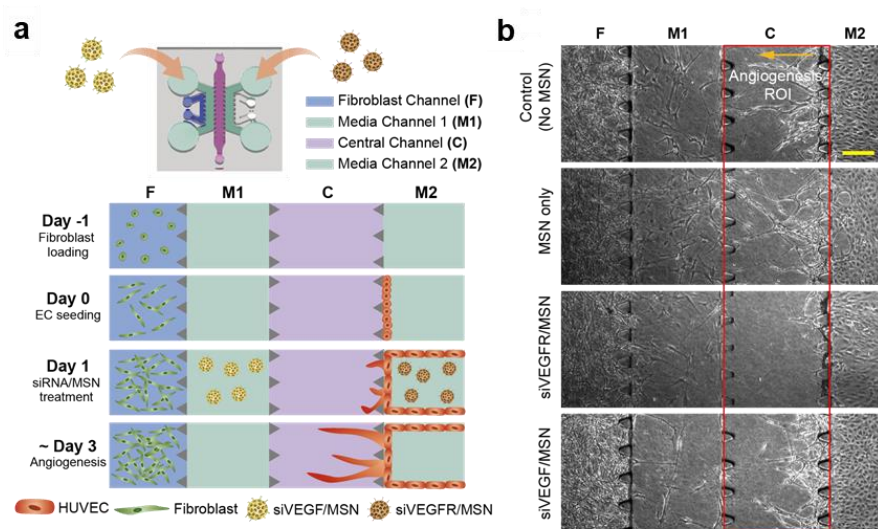
Figure 3.3. 3D microfluidic platform-based in vitro angiogenesis regulation by siVEGF/MSN or siVEGFR/MSN treatment. (a) Schematic overview of chip design for angiogenesis assay. Cell loading sequence is described as channel section view. (b) Representative brightfield images for each treatment condition. Red box indicates boundary of channel C where EC 3D sprouting happens and the direction of angiogenic sprouting is indicated as orange arrow. Scale bar is 200 μm.

Although the aforementioned data revealed the change in 3D angiogenic phenotype of genetically modified cells, this approach did not demonstrate the entire process of siRNA/MSN delivery within the 3D microenvironment. Since the delivery of siRNA/MSN to target cells could be influenced by extracellular matrix, vessel barrier, or flow variations,[120, 121] the valid evaluation of nanomedicine should be conducted in a model recapitulating those complex components of the microenvironment. Therefore, we designed an assay to administer siRNA/MSN to cells while being cultured in a 3D angiogenesis-on-a-chip (Figure 3.3). Cells were loaded with 3D fibrin hydrogel, then incubated overnight; siVEGF/MSN or siVEGFR/MSN was introduced for 6 h through the media channel the following day. We checked the viability of the EC layer on media channel M2 every day after nanomedicine treatment (Figure 3.3). There was no difference in the EC proliferation rate between the control and siRNA/MSN groups, which indicates that the nanomedicine treatment had no critical effect on EC viability. As described in Figure 3.3b, anti-angiogenic effect was prominently observed at the central channel (C) for samples treated with siVEGFR/MSN applied on media channel 2 (M2). In contrast, *in vitro* angiogenesis was not influenced by siVEGF/MSN treatment in media
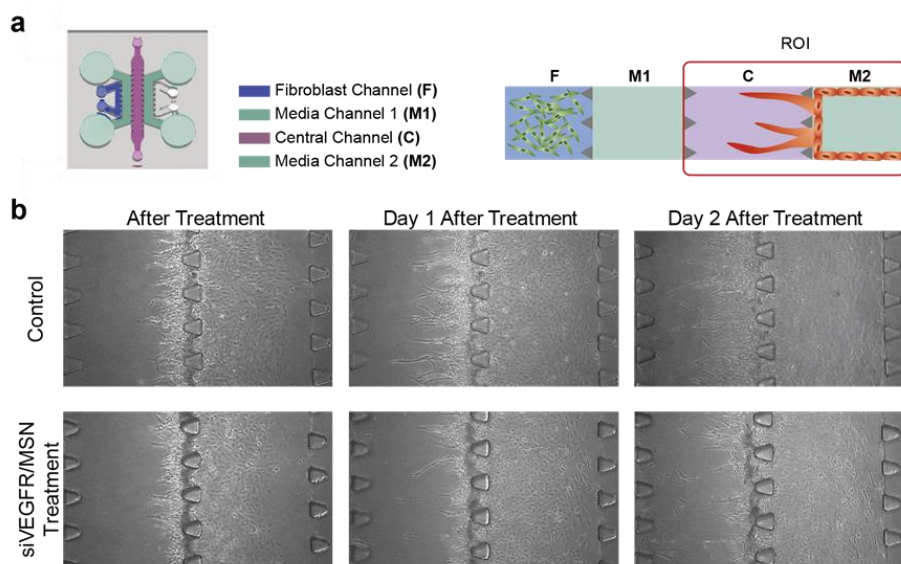
Figure 3.4. Day-by-day bright-field images of HUVEC in microfluidic device after nanomedicine treatment. Region of interest is set on central channel C and media channel M2 where HUVECs are directly exposed to nanomedicine. Scale bar is 200 μm.
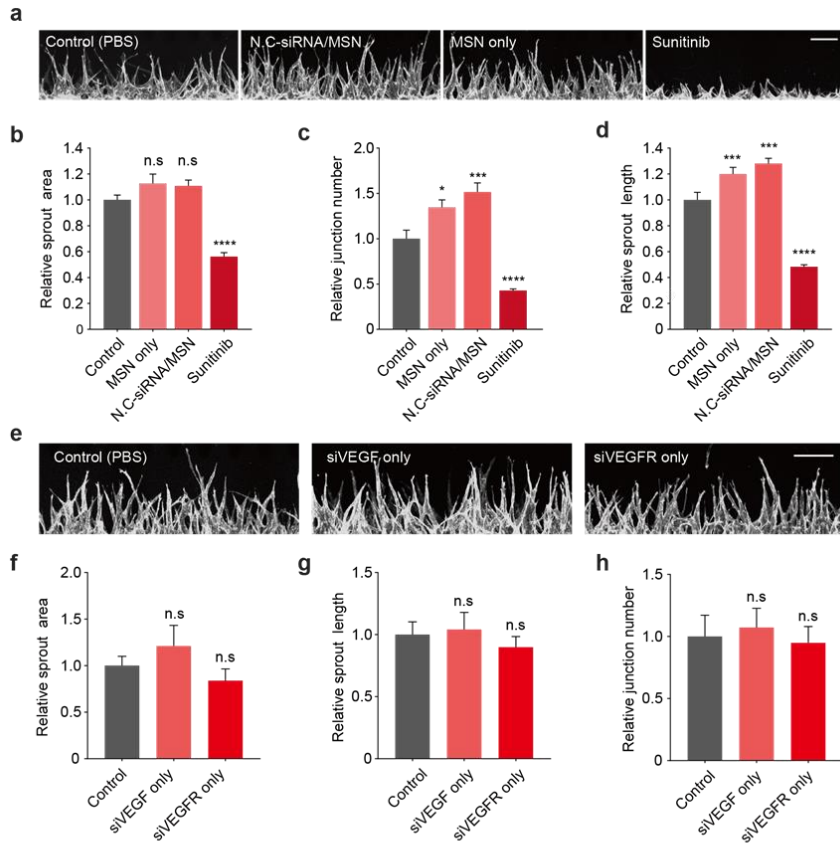
Figure 3.5. Evaluation of anti-angiogenic effect of diverse control groups. (a) Representative z-stacked confocal images of angiogenic sprouts in different control groups including MSN only and N.C-siRNA/MSN treatment as negative controls and Sunitinib treatment as positive control. (b), (c), (d) Quantitative analysis on sprouting area, junction number, and sprout length, respectively, relative to non-treated PBS group. (e) Representative z-stacked confocal images of angiogenic sprouts in different control groups including siVEGF only and siVEGFR only treatment as negative control. (f), (g), (h) Quantitative analysis on sprouting area, junction number, and sprout length, respectively, relative to non-treated PBS group. All scale bars are 200 μm. All measured value was normalized by the average of control (PBS) groups as 1. (*$p < 0.05$, **$p < 0.01$, ***$p < 0.001$, ****$p < 0.0001$, N.S. stans for not significant, One-way ANOVA with subsequent Tukey's multiple comparisons post-test, n = 6 to 8 for figure S7a experiment and n = 2 to 4 for figure S7e set.

channel 1 (M1), although it had been expected to reduce VEGF signaling from fibroblasts in the fibroblast channel (F), similar to a previous result in Figure 3.2. Diverse control groups were additionally tested for their effect on angiogenic sprouting. Compared to non-treated group, MSN only, N.C-siRNA/MSN, siVEGF only and siVEGFR only treated group did not show anti-angiogenic effect (Figure 3.5). On the other hand, treatment with Sunitinib (a small molecule VEGFR inhibitor, FDA approved) as positive control resulted in a significant decrease in angiogenic sprouting (Figure 3.5). Since siVEGFR/MSN treatment caused a significant change in angiogenic sprouting, we performed additional experiments to determine whether siVEGFR dosage might affect the sprout length of HUVECs. 3D confocal imaging of angiogenic sprouts on day 4 after HUVEC attachment revealed a reduction in sprout length for siVEGFR/MSN treated samples, compared to samples treated with MSN alone (Figure 3.3). The average length of cells treated with 2 × siVEGFR was 2.38-fold less than the average length of cells only treated with MSN itself without siVEGFR (Figure 3.3). Overall, we successfully verified the anti-angiogenic effect of siVEGFR/MSN using our proposed 3D microfluidic platform. Our results are consistent with the biological basis of VEGF/VEGFR signaling in angiogenesis. Since

VEGFR is mainly expressed on ECs, it could function as more a specific target compare to soluble VEGF family members secreted from diverse cell sources found in the TME such as fibroblasts, cancers, ECs, *etc.* In subsequent analysis, all cancer angiogenesis assays in this study using 3D cancer angiogenesis-on-a-chip and 3D vascular mapping on xenograft model focused on siVEGFR/MSN.

3.3.2. Regulation of 3D cancer angiogenesis *in vitro* by siVEGFR/MSN in microfluidic chip

Cancer angiogenesis is a major topic in pathological angiogenesis, as well as the most critical target of cancer therapeutics.[4, 5] Since cancer cells are a major source of pro-angiogenic factors such as VEGF, we applied cancer cell in microfluidic 3D angiogenesis assay to screen the effect of siVEGFR/MSN on cancer angiogenesis. Various types of cancer cells were 3D cultured on the tumor channel (T), next to the central channel (C) where ECs sprout out toward the cancer. Because the cancer cell line alone had no potential to generate 3D angiogenic sprouting in this platform, fibroblasts were applied on side channel F for all samples, thus providing a basal level of pro-angiogenic factors (Figure 3.6).

Screening of the angiogenic potentials of six different cancer cell lines
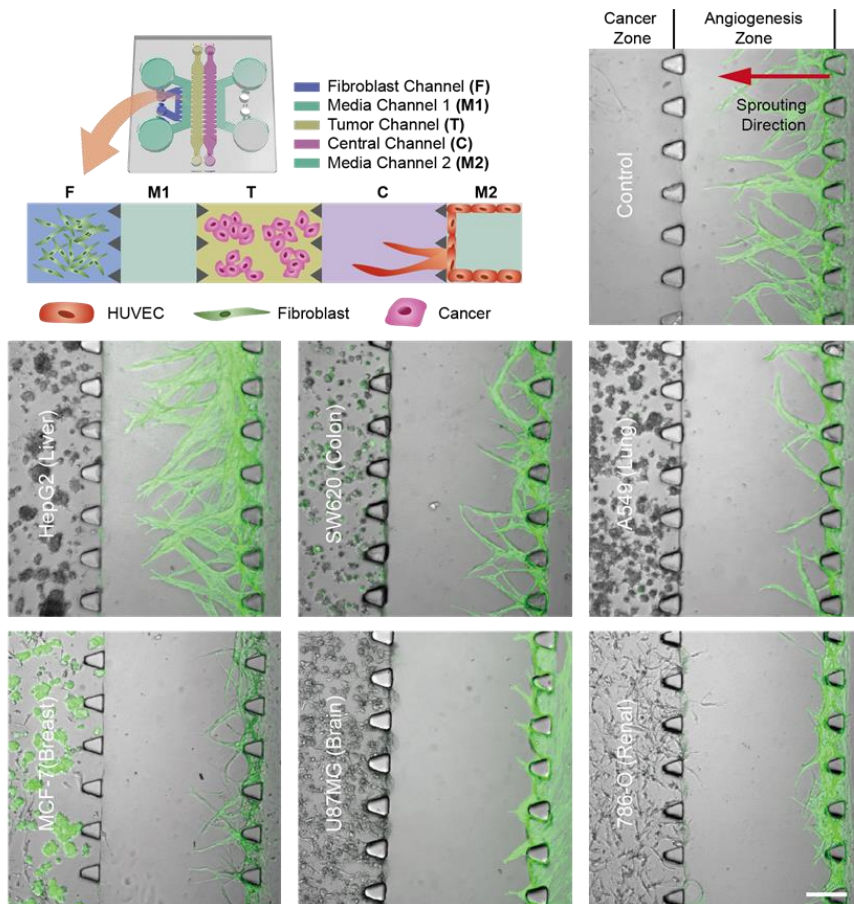
Figure 3.6. Screening on angiogenic potential of multiple cancer cell lines using 3D microfluidic cancer angiogenesis platform. Representative bright field image merged with confocal image of lectin (green). Scale bar is 200 μm.

was conducted in prior to testing effect of siVEGFR/MSN (Figure 3.6).

Previously in vascular biology researches, angiogenic heterogeneity has been reported among different cancer types.[122-124] In our microfluidic model, different angiogenic sprouting phenotype were observed in different cell lines (Figure 3.6). Compared to the condition with fibroblast alone, HepG2 cells showed a high degree of angiogenesis; angiogenesis was negatively affected in A549, MCF-7, U87MG, and 786-O cells. Based on the result of the screening assay, we chose HepG2, SW620, and A549 cell to represent various levels of angiogenic potential observed in our *in vitro* platform. Particularly, the cell line of hepatocellular carcinoma, HepG2, was used to simulate hyper-vascular TME.[125]

The cancer angiogenesis assay using 3D microfluidic model clearly revealed the anti-angiogenic effects of siVEGFR/MSN by 3D confocal imaging of the TME. As shown in figure 4b, we visualized the angiogenic sprouting of HUVECs (red) toward hepatocellular carcinoma HepG2 cells (green). Because of the 3D cell patterning in microfluidic platform, we were able to dissect the EC sprouting zone (central channel, C) and the cancer zone (tumor channel, T), which enabled a clear comparison of the anti-angiogenic effect between siVEGFR/MSN or
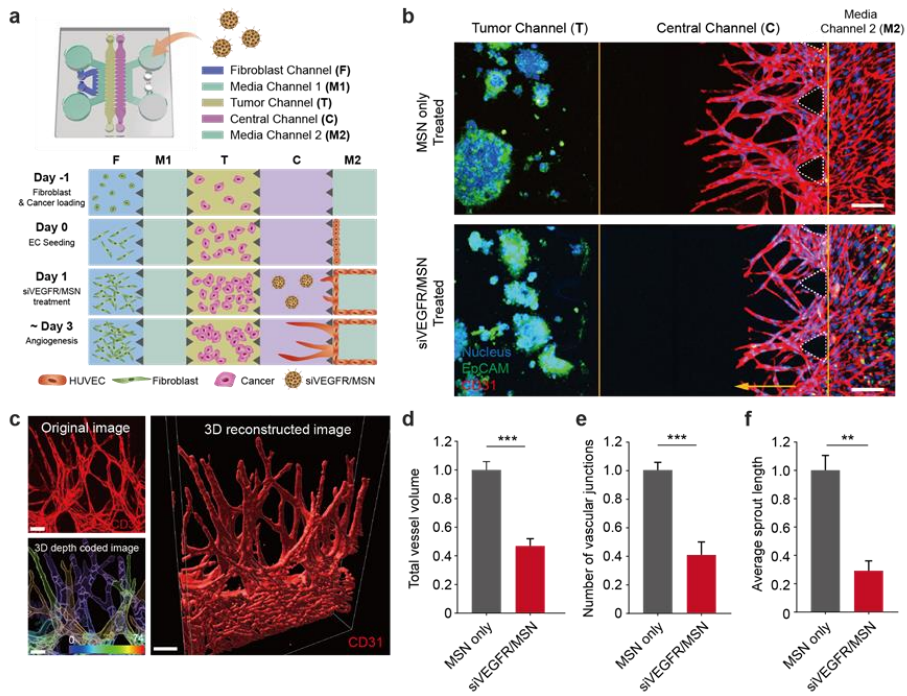
Figure 3.7. 3D microfluidic platform-based in vitro cancer angiogenesis regulation by siVEGFR/MSN treatment. (a) Schematic overview of chip design for cancer angiogenesis assay. Cell loading sequence is described as channel section view. (b) Representative confocal 3D image in orthogonal view of HepG2 angiogenesis assay with or without siVEGFR/MSN treatment. Yellow arrow in channel C indicates the direction of EC sprouting toward cancer cells. EpCAM (green), Nucleus (blue), and CD31 (red) immunostaining after day 4 culture. Scale bar is 200 μm. (c) 3D reconstructed confocal image of angiogenic sprouting. 3D depth coated image (top right) indicates each 3D sprouts in different depth point. Scale bar is 30 μm for top two images and 50 μm for bottom image. (d), (e), (f) Quantitative analysis on total vessel volume, average sprout length, and the number of vascular junctions of angiogenic sprouting co-cultured with HepG2. All measured value was normalized by the average of MSN Only condition as 1. (**p < 0.01, ***p < 0.001, unpaired t-test, n = 3 to 6 for each condition).
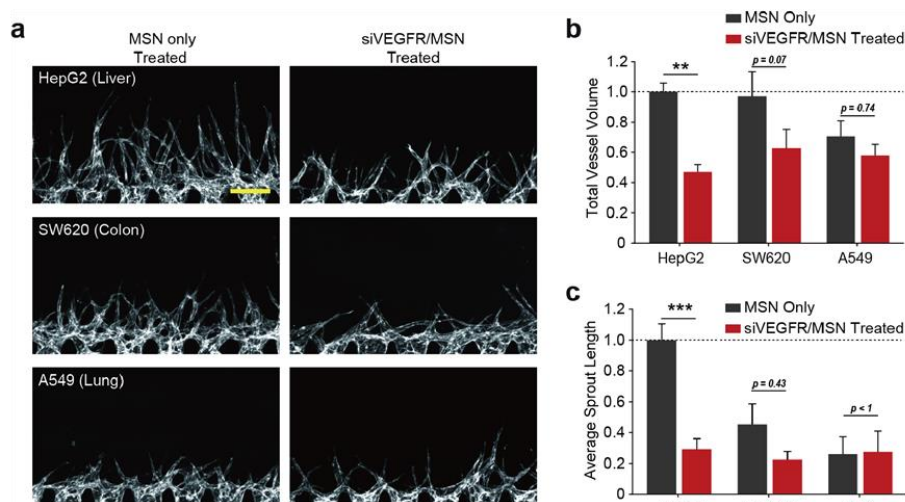
Figure 3.8. Evaluation of anti-angiogenic effect of siVEGFR/MSN depending on different co-cultured cancer types using microfluidic 3D cancer angiogenesis model. (a) Representative z-stacked confocal image of angiogenic sprouts in different cancer type conditions with MSNO only or siVEGFR/MSN treatment. Scale bar is 200 μm. (b) Quantitative analysis on total volume of vasculature in each culture and treatment condition. (c) Quantitative analysis on average length of vessel sprouts in each culture and treatment condition. All measured value was normalized by the average of MSN only treated condition as 1. (**p < 0.01, ***p < 0.001, Two-way ANOVA with subsequent Turkey's multiple comparisons post-test, n = 3 to 6 for each condition)

MSN only treated groups. Furthermore, 3D computational reconstruction of confocal image with depth coding verified that EC sprouted as multi-layered structure (Figure 3.7). Based on this computational 3D reconstruction, we conducted quantitative analysis on 3D angiogenic sprouts for each type of co-cultured cancer; HepG2, SW620 and A549. (Figure 3.8). Among them, HepG2 co-cultured condition showed significant reductions in total vessel volume, average sprout length, and the number of vascular junctions in siVEGFR/MSN treated groups compared to MSN only treated groups (Figure 3.8). In detail, siVEGFR/MSN treatment significantly resulted in a 2.13-fold less in total vessel volume, 3.43-fold less in average sprout length, and 2.44-fold less in the number of vascular junctions compared to MSN only treated groups. On the other hand, TME with SW620 or A549 had less or no significant effect on angiogenic phenotype in treatment of siVEGFR/MSN (Figure 3.8). The result implies the anti-angiogenic effect was more influential on TME with hyper-angiogenic cancer type. Since our 3D cancer angiogenesis model has successfully reconstituted the heterogeneity of cancer angiogenesis, it can help narrowing down the promising target of anti-angiogenic nanomedicine having cancer type-dependent efficacy. In particular, when compared to human vascular

organ-on-a-chip models developed by other groups [24, 100, 101, 103, 126-136], our model enables clearer visualization and quantification of unidirectional sprouting, which leads to an accurate comparison of the sprouting phenotype among different cancer types or treatment groups. Taken together, the 3D microfluidic platform is a powerful and efficient tool for evaluating the effect of anti-angiogenic nanomedicine. This phenotype evaluating system has the potential to provide rapid but reliable preclinical information that will contribute to successful nanomedicine development.

3.3.3. Systematic strategy for evaluating anti-angiogenic nanomedicine with multiple types of assays

Preclinical studies of RNAi-based nanomedicine targeting angiogenic pathways have been demonstrated as effective cancer therapeutics. However, the *in vitro* models or *in vivo* analytical methodology used in previous studies were not optimized for evaluating 3D angiogenic morphological phenotype. To address this problem, we implemented a robust strategy involving a 3D microfluidic cancer angiogenesis model and 3D imaging-based analysis. The proposed microfluidic platform

provided clear and intuitive visualization of directional 3D angiogenic sprouting toward cancer, by virtue of selective 3D cell patterning technology. Moreover, the system enabled efficient and rapid assessment of nanomedicine efficacy in hyper-angiogenic cancer within a reconstructed 3D TME, which afforded more reliable results when testing nanoparticle-delivered nanomedicine compared to classical 2D *in vitro* assays. In addition, the 3D imaging-based analysis enabled by tissue clearing technology offered precise visualization and assessment of the *in vivo* whole tumor vascular network with innate 3D structure; this approach did not require tissue sectioning. Based on broad morphological information with various parameters indicative of tumor vessel normalization, 3D imaging-based analysis could accurately evaluate the anti-angiogenic effects of nanomedicine.

In summary, our study provides an efficient strategy for reliable and accurate preclinical assessment of the anti-angiogenic efficacy of nanomedicine. Beyond siVEGF or siVEGFR nanomedicine particularly described in this study, we envision that this comprehensive and sequential evaluation, ranging from the molecular level to tissue level, could be applied to assess a broad range of nanomedicine designed for diverse pathologies. We presume that this systematic drug evaluation

process will aid in to the successful clinical application of RNAi-based nanomedicine.

3.3.4. Developing high-throughput tumor microenvironment

Modification of the device in Figure 3.9 provides a platform for convenient and effective comparison of paracrine signaling induced by co-culture of five cell types. Here, the microfluidic device contains four linear HRs surrounded by a square LR (Figure 3.10). Four support structures suspend the rail structures by connecting them to the well walls, which form growth medium reservoirs when bonded to a PSA film. Patterning of a fibrin hydrogel (2.5 mg/ml) containing a mixture of human umbilical vein endothelial cells (HUVEC, 4 x 10^6 cells/ml) and lung fibroblasts (LFs, 1 x 10^6 cells/ml) under the LR, and subsequent seeding of gels containing different cell types into the rendered microchannels establishes the basic experimental setup. The present studies involve eleven devices with channels containing different combinations of LFs, colon fibroblast cell line (CCD-18Co), liver cancer cell line (HepG2), glioblastoma cell line (U87MG), and lung carcinoma cell line (H1299). All gels contain cell concentrations of 5 x 10^6 cells/ml except for an acellular fibrin gel as a control. Figure 3.11a presents a
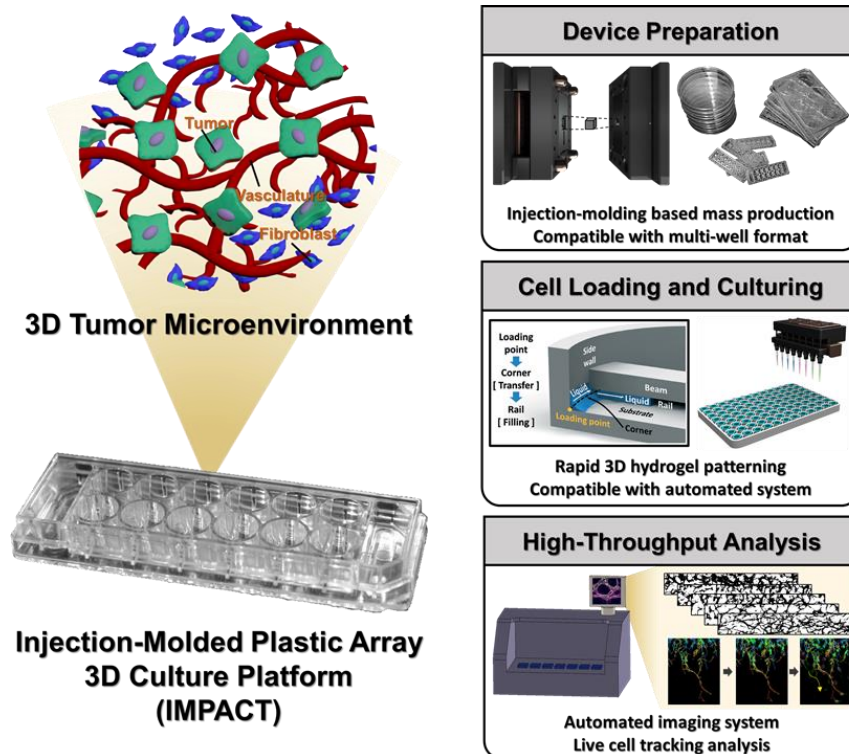
Figure 3.9. Schematic overview of Injection-Molded Plastic Array 3D Culture Platform (IMPACT) for generating in vitro 3D tumor microenvironment. Main technical properties of the platform on all experimental stages ranging from device fabrication to high-throughput analysis are described in right side. The figure describing the mechanism of capillary-guided liquid patterning is adapted with permission from Y. Lee et al., 2018.
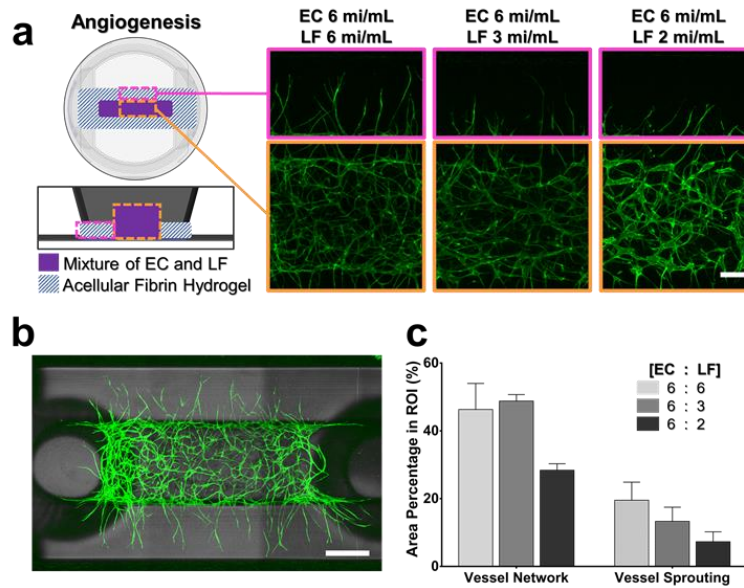
Figure 3.10. Angiogenesis assay on high-throughput injection-molded chip. (a) Illustration of patterning on the chip for angiogenesis assay. Confocal images of vasculature immunostained with anti-CD31 (green) in each condition having different concentration of HUVEC and LF. Network part and angiogenic sprouting part are separately presented in each concentration condition in orange box and pink box, respectively. (scale bar = 200 μm). (b) Representative 3D confocal image of angiogenic vasculature immunostained with anti-CD31 (green) merged with DIC image at the whole chip scale (scale bar = 500 μm). (c) Percentage of total vascular area in each concentration condition separately analyzed in center network part and round sprouting part, respectively. All error bars represent SD.

confocal image of an exemplary device taken after 5 days of cultivation. Regions of interest (ROI) measuring 1 x 1.8 mm^2 in area, which is located around each HR, encompass the interfaces between the HUVEC-LF gel and the gels containing cells of interest. Analysis of z-projected confocal images yield quantification of the vasculogenic capacities of the cells of interest (Figure 3.11d). In alignment with previous studies (*93, 100, 105*), LFs vigorously promote formation of vasculature. Furthermore, acellular gels and gels containing LFs exhibit angiogenic sprouting into the channels. On the other hand, U87MG and H1299 gels inhibit the growth of surrounding vessels and do not provoke cancer angiogenesis. Gels containing CCD-18Co and HepG2 show no significant difference in vasculogenic capacity compared against the acellular matrix. The results of these tests corroborate the ability of the platform for screening candidates for cancer angiogenesis *in vitro*. Furthermore, the versatility of the channel rendering method supports facile device adaptation to study a broad range of paracrine signaling cues in various conformations.

3.3.5. High-content profiling of angiogenic potential of multiple types of cancers using high-throughput tumor microenvrionment

system

Tumor cells are a source of vascular growth factor and stromal phenotype related signalling within the tumor microenvironment (TME), but the level and effects of these factors on vasculature varies between the different types of tumor.[122, 137] We demonstrated the application of our high-throughput co-culture platform to high-content profiling of the vasculogenic potential of nine different types of tumors. In order to facilitate multi-cell line type screening, the following cell lines were utilized: A549 (human adenocarcinomic human alveolar basal epithelial cells), BxPC3 (human adenocarcinomic pancreatic epithelial cells), HepG2 (human hepatocellular carcinoma), LoVo (human metastatic colorectal adenocarcinomic epithelial cell), SK-OV-3 (human adenocarcinomic ovarian epithelium), MCF7 (human mammary gland epithelial adenocarcinoma), U-87 MG (human glioblastoma), LNCaP (human prostate epithelial adenocarcinoma), and 786-O (human renal cell epithelial adenocarcinoma). Lung fibroblast co-culture was used as the control because it was optimized in previous studies[22, 24, 101] for the type of stromal cell to provide proangiogenic factors.[138] Each type of tumor or stromal cell (lung fibroblast) was
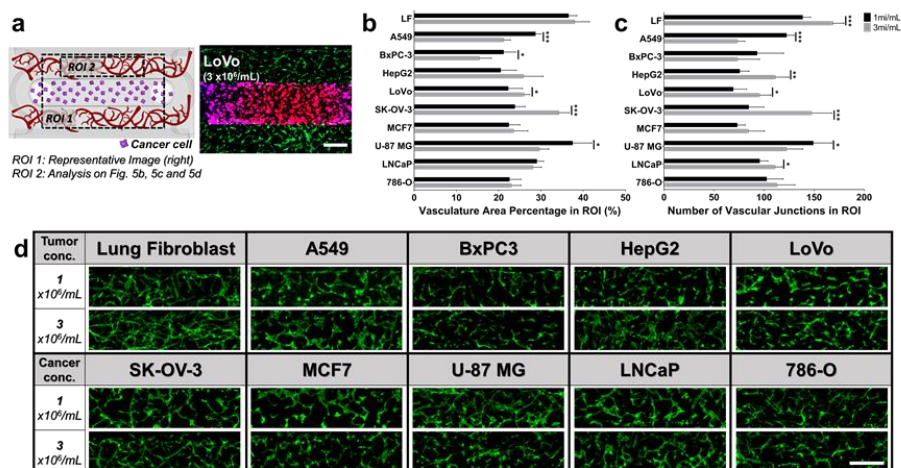
Figure 3.11. High-content profiling in tumor vasculature co-culture (a) Illustration of tumor vasculogenesis in IMPACT platform (left) and representative 3D confocal image (right) of whole cell loading part with tumor (LoVo, 3 $\times 10^6$/mL, red, anti-EpCAM) and vasculature (green, anti-CD31) (scale bar = 500 μm). (b) Percentage of total vasculature area among area of ROI in each co-culture condition. (c) The number of vascular junction in each co-culture condition. All error bars represent SD. (d) 3D confocal images of vasculature (green, anti-CD31) in ROI co-cultured with 9 different types of tumors and with stromal cells (Lung fibroblast) (scale bar = 500 μm).

loaded into the center channel with a 3D fibrin hydrogel at a concentration of 1 or 3 $\times 10^6$/mL, respectively. The round channel was loaded with HUVEC at a concentration of 6 $\times 10^6$/mL, and the cells were co-cultured for 3 days (Figure. 3.11). A representative confocal image of the vasculature in the region of interest (ROI, as shown in Figure. 3.11) of each co-culture condition is presented in Figure. 3.11d.

The morphology and distribution of the vasculature were highly characteristic of each tumor co-culture condition. The effect of the initial tumor cell concentration on vascular formation differed between the types of cells. The cell types A549, BxPC-3, HepG2, LoVo, SK-OV-3, and U-87 MG demonstrated tumor cell concentration-dependent differences in their vasculogenic effects on HUVECs. U-87 MG, for example, generated a less vasculogenic environment for HUVECs when cultured at 3 $\times 10^6$/mL than at 1 $\times 10^6$/mL. When examined in detail, the area of vasculature was 1.26-fold lower in the 3 $\times 10^6$/mL condition (29.54 ± 2.30 %) than in the 1 $\times 10^6$/mL condition (37.37 ± 4.63 %) (Figure. 3.12b). Additionally, the number of junctions was 1.22-fold lower in the 3 $\times 10^6$/mL condition (122.08 ± 16.64 on average) than in the 1

x10^6/mL condition (148.67 ± 19.03 on average; Figure. 3.12c). In contrast, SK-OV-3 cells generated a more vasculogenic microenvironment at a higher concentration (3 x10^6/mL), which resulted in the formation of vasculature that was more highly networked compared to the co-culture condition with a lower tumor cell concentration (1 x10^6/mL; Figure. 3.11). A quantitative analysis of both the area of vasculature and the number of junctions (Figure. 3.11) was also performed; the results indicated that these values were significantly higher when the co-culture contained a higher concentration of tumor cells. In contrast, vasculogenesis in the MCF7, LNCaP, and 786-O co-cultures showed little dependency on the tumor cell concentration.

In investigating differences in the effects of the tumor cell type on vasculogenesis, the most distinctive characteristic of the vasculature was the degree of vessel connectivity. Therefore, the branching ability was analyzed by quantifying the number of junctions in each co-culture condition (Figure. 3.11). All of the vasculatures co-cultured with tumor cells had less connectivity than that co-cultured with lung fibroblasts. In particular, the vasculatures co-cultured with BxPC3, LoVo, or MCF7 cells demonstrated poor

vessel connectivity and almost failed to form fully connected vasculature inside the chip.

The high-throughput assay using the platform enabled high-content profiling of the characteristics of the co-culturing of tumor cells and EC in a single set of experiments. The diverse analytic parameters of the vasculature represented the morphological differences between multiple co-culture conditions, and a consistent result was generated within each single co-culture condition. Analysis of the vasculature in the context of different tumor cell co-culture microenvironments will provide crucial information to enable accurate interpretation of tumor pathology. Beyond tumor cell vasculature co-cultures, the platform has potential for use as a screening tool to test the effects of single or multiple biological components on the 3D tissue microenvironment.

3.3.6. Testing multiple drugs using high-throughput tumor microenvrionment system

A variety of anti-tumor drugs have been applied to tumor therapy that utilize varying modes of action, including antiangiogenic

therapy, antimetabolite drugs, and immunotherapy. To investigate the different anti-tumor effects of different types of tumor therapy on a specific tumor type, we incorporated into the platform the human colorectal cancer (CRC) cell line LoVo, which is a model for the third most common tumor in the world.[139] Using the platform to culture a vascular network with tumor cells (Figure. 3.12a), we tested several anti-tumor drugs with different mechanisms: 5-FU, a conventionally prescribed[140] thymidylate synthesis inhibition mediated cell cycle inhibitor[141], Axitinib as an antiangiogenic drug that inhibits vascular endothelial growth factor (VEGF) receptor tyrosine kinases[142], which have been investigated for applications on treating advanced K-RAS mutant colorectal cancer[143] and Cetuximab, a chimeric IgG1 monoclonal antibody that binds to EGFR[144] with established treatment usage for non-K-RAS mutant colorectal cancer.[145] Additionally, in the case of Cetuximab, KRAS mutation of the tumor is known to lead to the absence of a cellular response to this drug.[146] The varying concentrations of each drug component were based on the dosage used in clinical treatments. The platform
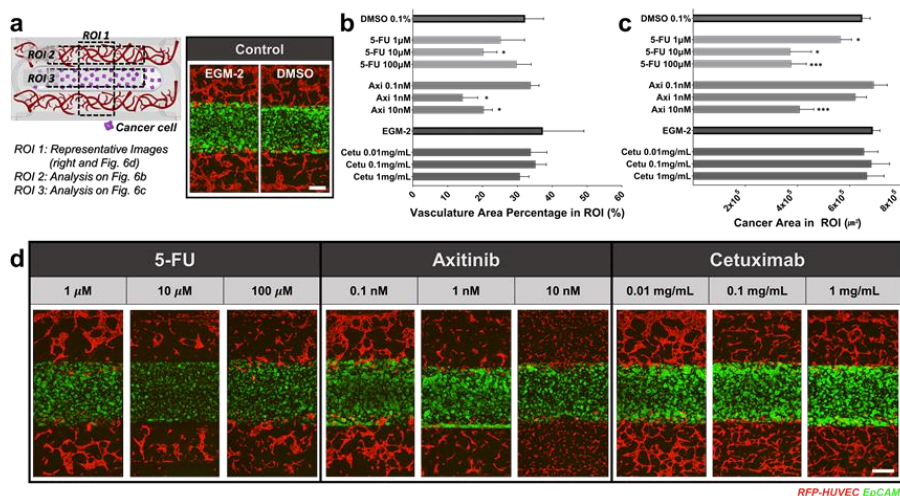
Figure 3.12. Drug screening targeting CRC using IMPACT platform (a) Illustration of tumor vasculogenesis in IMPACT platform (left) and confocal image (right) of control condition where tumor and blood vessel are cultured for 96 hours in EGM-2 and DMSO 0.1%, respectively (scale bar = 300 μm). (b) Confocal image of tumor and blood vessel (scale bar = 300 μm), (c) vasculature area percentage in ROI and (d) EpCAM expression area of tumor cells in IMPACT platform when treated with 5-FU, Axitinib and Cetuximab respectively with varying concentration of each drug.

was exposed to the drugs for 96 hours. Figure. 3.12b shows the response of blood vessels and tumor cells in the ROI to each type of drug and its concentration. To quantify each of the cellular responses to the varying doses of the respective drug type, graphs of the vasculature area percentage in the ROI and the area of EpCAM expression of the CRC are shown in Figure. 3.12.

For the 5-FU treatment, the area of EpCAM expression in the tumor cells significantly decreased as the dose of 5-FU increased ($5.72 \times 10^5 \pm 3.62 \times 10^4$, $3.7 \times 10^5 \pm 8.27 \times 10^4$, and $3.38 \times 10^5 \pm 3.52 \times 10^4$ μm^2 for 1, 10, and 100 μM 5-FU, respectively), as compared to the control ($6.45 \times 10^5 \pm 3.34 \times 10^4$ μm^2 for 0.1% DMSO). The area percent of the blood vessels in the ROI significantly decreased when the platform was exposed to 10 μM 5-FU (20.08 ± 4.05 %), whereas there was no significant change in these values when it was exposed to 1 μM (25.05 ± 7.01 %) or 100 μM (29.61 ± 4.34 %) 5-FU, as compared to the control (32.00 ± 5.49 % in 0.1% DMSO). As a cytotoxic drug, 5-FU affects not only the blood vascular network, but also EpCAM expression of the CRC at a certain drug concentration.

When the microvascular network cultured with the CRC in the

platform was treated with 0.1 or 1 nM of Axitinib, there was no significant change in the level of EpCAM expression for the tumor cells ($6.89 \times 10^5 \pm 5.42 \times 10^4$ and $6.2 \times 10^5 \pm 4.49 \times 10^4$ μm^2 in 0.1 or 1 nM Axitinib, respectively), as compared to the control (0.1% DMSO). After treatment with 10 nM Axitinib, the area of EpCAM expressed on the tumor cells was significantly reduced ($4.3 \times 10^5 \pm 3.99 \times 10^4$ μm^2). However, the percent of the microvascular network area had significantly decreased after 96 hours of exposure to 1 or 10 nM Axitinib (14.11 ± 4.53 and 20.15 ± 2.63 %, respectively), and the vasculature area was not significantly different from that of the control (0.1% DMSO) when exposed to 0.1 nM Axitinib ($33.64 \pm 2.58\%$).

Interestingly, the changes in the vasculature area ($37.08 \pm 12.01\%$ in EGM-2) and EpCAM expression ($6.85 \times 10^5 \pm 3.01 \times 10^4$ μm^2 in EGM-2) were moderate when Cetuximab was applied to the platform, regardless of the concentration compared to the control (EGM-2). For tumor cells, EpCAM expression of the tumor cells was $6.8 \times 10^5 \pm 1.88 \times 10^4$, $6.81 \times 10^5 \pm 7.23 \times 10^4$, and $6.99 \times 10^5 \pm 6.11 \times 10^4$ μm^2 after exposing the platform to 0.01, 0.1, or 1 mg/mL of Cetuximab, respectively. For the vascular network, the

percentage of the vasculature area in the ROI was 33.64 ± 4.85, 34.98 ± 3.30, or 30.54 ± 2.78 % after treatment with 0.01, 0.1, or 1 mg/mL Cetuximab, respectively. Unlike 5-FU and Axitinib, the change in the response of LoVo, a KRAS mutant CRC cell line, to Cetuximab exposure was minimal regardless of the concentration of the drug.[147, 148] By testing a variety of therapeutic drugs at varying concentrations using this platform, each cellular response can be readily observed, quantified, and analyzed.

3.4. Conclusions

Preclinical studies of anti-angiogenic medicines have been demonstrated them as effective cancer therapeutics. However, the *in vitro* models or *in vivo* analytical methodology used in previous studies were not optimized for evaluating 3D angiogenic morphological phenotype. To address this problem, me and my collaborative research team implemented a robust strategy involving a 3D microfluidic cancer angiogenesis model and 3D imaging-based analysis. The proposed microfluidic platform provided clear and intuitive visualization of directional 3D angiogenic sprouting toward cancer, by virtue of selective 3D cell patterning technology. Moreover, the system enabled efficient

and rapid assessment of nanomedicine efficacy in hyper-angiogenic cancer within a reconstructed 3D TME, which afforded more reliable results when testing nanoparticle-delivered nanomedicine compared to classical 2D *in vitro* assays.

In summary, our study provides an efficient strategy for reliable and accurate preclinical assessment of the anti-angiogenic efficacy of nanomedicine. Beyond siVEGF or siVEGFR nanomedicine particularly described in this study, we envision that this comprehensive and sequential evaluation, ranging from the molecular level to tissue level, could be applied to assess a broad range of nanomedicine designed for diverse pathologies. We presume that this systematic drug evaluation process will aid in to the successful clinical application of RNAi-based nanomedicine.

Also, the high-throughput injection-molded platform is capable of robustly patterning up to four different compartments with cell laden/acellular hydrogel compositions and cell suspensions in any number of combinations and configurations for the production of a highly modular experimental platform. We utilized this versatile system to co-culture heterogeneous vasculature comprised of different cell types and concentrations and organizations of components to engineer

controllable and quantifiable vascular networks. We established controlled drug treatment schemes of engineered co-cultures of vascular tissue and tumor cells, and quantified dose-dependent and target-dependent responses to each drug type.

Chapter 4. Concluding Remarks

Preclinical study is the most fundamental step in the drug discovery process, which filters the most appropriate drug candidate with high efficacy and safety before the clinical trial. Numerous *in vivo* and *in vitro* models, ranging from simple 2D dish culture to complex 3D tissue culture, were introduced as preclinical models. In vascular biology, studying pathological angiogenesis and regulating abnormal angiogenesis has been the crucial point in various tissue physiopathology, including cancer. During my Ph.D. course, I have developed the microphysiological systems (MPSs) recapitulating the critical function and pathology of angiogenesis.

First, I reported a novel 3D *in vitro* BBB model that mimicked the development of CNS angiogenesis. This strategy relies on the biological knowledge that the maturation of BBB barrier phenotypes occurs during CNS angiogenesis, which is different from typical vasculature development in other tissues. In this platform, primary human brain ECs exhibited BBB phenotypes such as narrow vascular morphology, high tight junction expression, low permeability, and functional efflux transporter system only when co-cultured with both perivascular cells.

This model allows us to observe the penetration of molecules through the luminal part of blood vessels under 3D conditions. I believe this model has strong potential for research on the transport characteristics of CNS drugs.[149] Moreover, since the model is based on a quantitative angiogenesis assay, it can be used to evaluate CNS medications targeting pathological angiogenesis associated with a brain tumor[150] or brain damage.[151, 152] Combining this BBB tissue engineering with the emerging technology of high-throughput screening systems[98, 153] will permit the practical use of this model in preclinical tests and translational research, to develop improved CNS medications in the near future. This study was published in Biotechnology and Bioengineering, and it was reused in this thesis with the publisher's permission.[136]

As cancer angiogenesis is the most popular indicator of tumor progress, as well as most abundantly regarded as the target of cancer therapeutics, there is a high demand for optimal MPS to evaluate the efficacy of anti-angiogenic drugs. Preclinical studies of RNAi-based nanomedicine targeting angiogenic pathways have also been demonstrated as effective cancer therapeutics. However, the *in vitro* models or *in vivo* analytical methodology used in previous studies were not optimized for evaluating 3D angiogenic morphological phenotype. To address this problem, me

and my collaborative researchers from the biology and chemical department implemented a robust strategy involving a 3D microfluidic cancer angiogenesis model and 3D imaging-based analysis. The proposed microfluidic platform provided clear and intuitive visualization of directional 3D angiogenic sprouting toward cancer by virtue of selective 3D cell patterning technology. Moreover, the system enabled efficient and rapid assessment of nanomedicine efficacy in hyper-angiogenic cancer within a reconstructed 3D TME, which afforded more reliable results when testing nanoparticle-delivered nanomedicine compared to classical 2D *in vitro* assays. Our study provided an efficient strategy for reliable and accurate preclinical assessment of the anti-angiogenic efficacy of nanomedicine. Beyond siVEGF or siVEGFR nanomedicine particularly described in this study, we envision that this comprehensive and sequential evaluation, ranging from the molecular level to tissue level, could be applied to assess a broad range of nanomedicine designed for diverse pathologies. We presume that this systematic drug evaluation process will aid in to the successful clinical application of RNAi-based nanomedicine. This study was published in ACS Nano, and it was reused in this thesis with the publisher's permission.[154]

To extend the use of the MPS from drug efficacy evaluation to high-throughput drug screening, I developed a high-throughput platform for generating robust samples for a drug test. Injection molding-based plastic chip designing and fabrication enabled maximization of the assay, which was a common limitation for the assays based on PDMS chip. By developing the high-throughput tumor vascular model[98, 155], I proved this MPS model could apply on high-content profiling of heterogeneous angiogenic potential of multiple cancer types and the effect of anti-cancer drugs with diverse mechanisms on tumor vasculature. This study has suggested the concept and future perspective of how MPS should be designed to fulfill the need of the pharmaceutical community in the near future. This study was published in Lab on a Chip, and it was reused in this thesis with the publisher's permission.[98]

In conclusion, 3D angiogenesis in human pathophysiology was recapitulating using 3D microfluidic MPS. Ranging from the organotypic function of brain vasculature to regulation in cancer angiogenesis through anti-angiogenic drug, the model enables quantitative and physiologically relevant analysis on human 3D angiogenic sprouting. Moreover, as the trend of MPS is seeking the maximization of throughput in the assay, high-throughput MPS for

evaluating the anti-angiogenic or anti-cancer therapeutics is now being developed, including the mass-producible plastic array chip. Through introducing extensive researches on modeling and applying 3D angiogenesis MPS in diverse preclinical studies, this Ph.D. thesis suggests the powerful potential of the platform to provide efficient and reliable solutions in various biomedical research fields in the near future.

Bibliography

1.   R. H. Adams and K. Alitalo, *Nat Rev Mol Cell Biol*, 2007, **8**, 464-478.
2.   S. P. Herbert and D. Y. Stainier, *Nat Rev Mol Cell Biol*, 2011, **12**, 551-564.
3.   H. G. Augustin and G. Y. Koh, *Science*, 2017, **357**.
4.   P. Carmeliet and R. K. Jain, *nature*, 2000, **407**, 249-257.
5.   P. Carmeliet, *Nature*, 2005, **438**, 932-936.
6.   M. Fernández, D. Semela, J. Bruix, I. Colle, M. Pinzani and J. Bosch, *Journal of hepatology*, 2009, **50**, 604-620.
7.   A. H. Vagnucci Jr and W. W. Li, *The Lancet*, 2003, **361**, 605-608.
8.   J. Folkman, *Journal of the National Cancer Institute: JNCI.*, 1990, **82**, 4.
9.   F. Shojaei, *Cancer letters*, 2012, **320**, 130-137.
10.   S. M. Weis and D. A. Cheresh, *Nature medicine*, 2011, **17**, 1359.
11.   B. Sitohy, J. A. Nagy and H. F. Dvorak, *Cancer research*, 2012, **72**, 1909-1914.
12.   N. Ferrara, K. J. Hillan, H.-P. Gerber and W. Novotny, *Nature reviews Drug discovery*, 2004, **3**, 391-400.
13.   N. Ferrara, K. J. Hillan and W. Novotny, *Biochemical and biophysical research communications*, 2005, **333**, 328-335.
14.   N. Ferrara and R. S. Kerbel, *Nature*, 2005, **438**, 967-974.
15.   M. Yi, D. Jiao, S. Qin, Q. Chu, K. Wu and A. Li, *Molecular cancer*, 2019, **18**, 60.
16.   P. Nowak-Sliwinska, K. Alitalo, E. Allen, A. Anisimov, A. C. Aplin, R. Auerbach, H. G. Augustin, D. O. Bates, J. R. van Beijnum, R. H. F. Bender, G. Bergers, A. Bikfalvi, J. Bischoff, B. C. Bock, P. C. Brooks, F. Bussolino, B. Cakir, P. Carmeliet, D. Castranova, A. M. Cimpean, O. Cleaver, G. Coukos, G. E. Davis, M. De Palma, A. Dimberg, R. P. M. Dings, V. Djonov, A. C. Dudley, N. P. Dufton, S. M. Fendt, N. Ferrara, M. Fruttiger, D. Fukumura, B. Ghesquiere, Y. Gong, R. J. Griffin, A. L. Harris, C. C. W. Hughes, N. W. Hultgren, M. L. Iruela-Arispe, M. Irving, R. K. Jain, R. Kalluri, J. Kalucka, R. S. Kerbel, J. Kitajewski, I.

Klaassen, H. K. Kleinmann, P. Koolwijk, E. Kuczynski, B. R. Kwak, K. Marien, J. M. Melero-Martin, L. L. Munn, R. F. Nicosia, A. Noel, J. Nurro, A. K. Olsson, T. V. Petrova, K. Pietras, R. Pili, J. W. Pollard, M. J. Post, P. H. A. Quax, G. A. Rabinovich, M. Raica, A. M. Randi, D. Ribatti, C. Ruegg, R. O. Schlingemann, S. Schulte-Merker, L. E. H. Smith, J. W. Song, S. A. Stacker, J. Stalin, A. N. Stratman, M. Van de Velde, V. W. M. van Hinsbergh, P. B. Vermeulen, J. Waltenberger, B. M. Weinstein, H. Xin, B. Yetkin-Arik, S. Yla-Herttuala, M. C. Yoder and A. W. Griffioen, *Angiogenesis*, 2018, **21**, 425-532.

17.   G. M. Palmer, A. N. Fontanella, S. Shan, G. Hanna, G. Zhang, C. L. Fraser and M. W. Dewhirst, *Nature protocols*, 2011, **6**, 1355.

18.   R. Rust, L. Gronnert, B. Dogancay and M. E. Schwab, *Sci Rep*, 2019, **9**, 3263.

19.   A. Stamm, K. Reimers, S. Strauß, P. Vogt, T. Scheper and I. Pepelanova, *BioNanoMaterials*, 2016, **17**.

20.   S. Lee, J. Ko, D. Park, S. R. Lee, M. Chung, Y. Lee and N. L. Jeon, *Lab Chip*, 2018, DOI: 10.1039/c8lc00285a.

21.   V. van Duinen, S. J. Trietsch, J. Joore, P. Vulto and T. Hankemeier, *Curr Opin Biotechnol*, 2015, **35**, 118-126.

22.   S. Kim, M. Chung, J. Ahn, S. Lee and N. L. Jeon, *Lab on a Chip*, 2016, **16**, 4189-4199.

23.   A. C. Newman, M. N. Nakatsu, W. Chou, P. D. Gershon and C. C. Hughes, *Mol Biol Cell*, 2011, **22**, 3791-3800.

24.   S. Kim, H. Lee, M. Chung and N. L. Jeon, *Lab on a Chip*, 2013, **13**, 1489-1500.

25.   W. A. Banks, *Nat Rev Drug Discov*, 2016, **15**, 275-292.

26.   B. Obermeier, R. Daneman and R. M. Ransohoff, *Nat Med*, 2013, **19**, 1584-1596.

27.   N. J. Abbott, A. A. Patabendige, D. E. Dolman, S. R. Yusof and D. J. Begley, *Neurobiol Dis*, 2010, **37**, 13-25.

28.   N. J. Abbott, L. Ronnback and E. Hansson, *Nat Rev Neurosci*, 2006, **7**, 41-53.

29.   B. Engelhardt, *Cell Tissue Res*, 2003, **314**, 119-129.

30.   M. Vallon, J. Chang, H. Zhang and C. J. Kuo, *Cell Mol Life Sci*,

2014, **71**, 3489-3506.

31. R. A. Umans, H. E. Henson, F. Mu, C. Parupalli, B. Ju, J. L. Peters, K. A. Lanham, J. S. Plavicki and M. R. Taylor, *Dev Biol*, 2017, **425**, 101-108.

32. S. Nakagawa, M. A. Deli, H. Kawaguchi, T. Shimizudani, T. Shimono, A. Kittel, K. Tanaka and M. Niwa, *Neurochem Int*, 2009, **54**, 253-263.

33. S. Nakagawa, M. A. Deli, S. Nakao, M. Honda, K. Hayashi, R. Nakaoke, Y. Kataoka and M. Niwa, *Cell Mol Neurobiol*, 2007, **27**, 687-694.

34. K. Hatherell, P. O. Couraud, I. A. Romero, B. Weksler and G. J. Pilkington, *J Neurosci Methods*, 2011, **199**, 223-229.

35. R. Booth and H. Kim, *Lab Chip*, 2012, **12**, 1784-1792.

36. A. K. Achyuta, A. J. Conway, R. B. Crouse, E. C. Bannister, R. N. Lee, C. P. Katnik, A. A. Behensky, J. Cuevas and S. S. Sundaram, *Lab Chip*, 2013, **13**, 542-553.

37. J. A. Brown, V. Pensabene, D. A. Markov, V. Allwardt, M. D. Neely, M. Shi, C. M. Britt, O. S. Hoilett, Q. Yang, B. M. Brewer, P. C. Samson, L. J. McCawley, J. M. May, D. J. Webb, D. Li, A. B. Bowman, R. S. Reiserer and J. P. Wikswo, *Biomicrofluidics*, 2015, **9**, 054124.

38. L. M. Griep, F. Wolbers, B. de Wagenaar, P. M. ter Braak, B. B. Weksler, I. A. Romero, P. O. Couraud, I. Vermes, A. D. van der Meer and A. van den Berg, *Biomed Microdevices*, 2013, **15**, 145-150.

39. K. L. Sellgren, B. T. Hawkins and S. Grego, *Biomicrofluidics*, 2015, **9**, 061102.

40. J. D. Wang, S. Khafagy el, K. Khanafer, S. Takayama and M. E. ElSayed, *Mol Pharm*, 2016, **13**, 895-906.

41. H. Cho, J. H. Seo, K. H. Wong, Y. Terasaki, J. Park, K. Bong, K. Arai, E. H. Lo and D. Irimia, *Sci Rep*, 2015, **5**, 15222.

42. A. Herland, A. D. van der Meer, E. A. FitzGerald, T. E. Park, J. J. Sleeboom and D. E. Ingber, *PLoS One*, 2016, **11**, e0150360.

43. G. Adriani, D. Ma, A. Pavesi, R. D. Kamm and E. L. Goh, *Lab Chip*, 2017, **17**, 448-459.

44. S. Bang, S. R. Lee, J. Ko, K. Son, D. Tahk, J. Ahn, C. Im and N. L. Jeon, *Sci Rep*, 2017, **7**, 8083.

45. S. R. Lee, S. Hyung, S. Bang, Y. Lee, J. Ko, S. Lee, H. J. Kim and N. L. Jeon, *Biofabrication*, 2019, **11**, 035013.

46. M. Campisi, Y. Shin, T. Osaki, C. Hajal, V. Chiono and R. D. Kamm, *Biomaterials*, 2018, **180**, 117-129.

47. S. Liebner, C. J. Czupalla and H. Wolburg, *Int J Dev Biol*, 2011, **55**, 467-476.

48. R. Daneman, D. Agalliu, L. Zhou, F. Kuhnert, C. J. Kuo and B. A. Barres, *Proc Natl Acad Sci U S A*, 2009, **106**, 641-646.

49. S. Kim, H. Lee, M. Chung and N. L. Jeon, *Lab Chip*, 2013, **13**, 1489-1500.

50. M. Ramsauer, D. Krause and R. Dermietzel, *FASEB J*, 2002, **16**, 1274-1276.

51. L. G. Dubois, L. Campanati, C. Righy, I. D'Andrea-Meira, T. C. Spohr, I. Porto-Carreiro, C. M. Pereira, J. Balca-Silva, S. A. Kahn, M. F. DosSantos, A. Oliveira Mde, A. Ximenes-da-Silva, M. C. Lopes, E. Faveret, E. L. Gasparetto and V. Moura-Neto, *Front Cell Neurosci*, 2014, **8**, 418.

52. Y. Yao, Z. L. Chen, E. H. Norris and S. Strickland, *Nat Commun*, 2014, **5**, 3413.

53. A. ElAli, P. Theriault and S. Rivest, *Int J Mol Sci*, 2014, **15**, 6453-6474.

54. N. B. Hamilton, D. Attwell and C. N. Hall, *Front Neuroenergetics*, 2010, **2**.

55. A. Zozulya, C. Weidenfeller and H. J. Galla, *Brain Res*, 2008, **1189**, 1-11.

56. A. Armulik, G. Genove, M. Mae, M. H. Nisancioglu, E. Wallgard, C. Niaudet, L. He, J. Norlin, P. Lindblom, K. Strittmatter, B. R. Johansson and C. Betsholtz, *Nature*, 2010, **468**, 557-561.

57. H. Kusuhara, H. Suzuki, T. Terasaki, A. Kakee, M. Lemaire and Y. Sugiyama, *Journal of Pharmacology and Experimental Therapeutics*, 1997, **283**, 574-580.

58. A. Mishra, F. M. O'Farrell, C. Reynell, N. B. Hamilton, C. N. Hall and D. Attwell, *Nat Protoc*, 2014, **9**, 323-336.

59. A. D. Wong, M. Ye, A. F. Levy, J. D. Rothstein, D. E. Bergles and P. C. Searson, *Front Neuroeng*, 2013, **6**, 7.

60. D. S. Miller, B. Bauer and A. M. Hartz, *Pharmacol Rev*, 2008, **60**, 196-209.

61. A. H. Schinkel, *Advanced Drug Delivery Reviews*, 1999, **36**, 179-194.

62. A. Tsuji and I. Tamai, *Advanced Drug Delivery Reviews*, 1997, **25**, 287-298.

63. Z. Holló, L. Homolya, C. W. Davis and B. Sarkadi, *Biochimica et Biophysica Acta (BBA) - Biomembranes*, 1994, **1191**, 384-388.

64. F. Tiberghien and F. Loor, *Anticancer Drugs*, 1996, **7**, 568-578.

65. H. Lee, S. Kim, M. Chung, J. H. Kim and N. L. Jeon, *Microvasc Res*, 2014, **91**, 90-98.

66. A. G. de Boer, I. C. van der Sandt and P. J. Gaillard, *Annu Rev Pharmacol Toxicol*, 2003, **43**, 629-656.

67. A. H. Schinkel, J. J. M. Smit, O. van Tellingen, J. H. Beijnen, E. Wagenaar, L. van Deemter, C. A. A. M. Mol, M. A. van der Valk, E. C. Robanus-Maandag, H. P. J. te Riele, A. J. M. Berns and P. Borst, *Cell*, 1994, **77**, 491-502.

68. M. R. Jablonski, S. S. Markandaiah, D. Jacob, N. J. Meng, K. Li, V. Gennaro, A. C. Lepore, D. Trotti and P. Pasinelli, *Ann Clin Transl Neurol*, 2014, **1**, 996-1005.

69. J. P. Bankstahl, M. Bankstahl, K. Romermann, T. Wanek, J. Stanek, A. D. Windhorst, M. Fedrowitz, T. Erker, M. Muller, W. Loscher, O. Langer and C. Kuntner, *Drug Metab Dispos*, 2013, **41**, 754-762.

70. S. Bihorel, G. Camenisch, M. Lemaire and J. M. Scherrmann, *J Neurochem*, 2007, **102**, 1749-1757.

71. D. G. Kim and M. S. Bynoe, *J Clin Invest*, 2016, **126**, 1717-1733.

72. P. J. Gaillard, I. C. J. van der Sandt, L. H. Voorwinden, D. Vu, J. L. Nielsen, A. G. de Boer and D. D. Breimer, *Pharmaceutical Research*, 2000, **17**, 1198-1205.

73. C. F. Cho, J. M. Wolfe, C. M. Fadzen, D. Calligaris, K. Hornburg, E. A. Chiocca, N. Y. R. Agar, B. L. Pentelute and S. E. Lawler, *Nat Commun*, 2017, **8**, 15623.

74. S. Bergmann, S. E. Lawler, Y. Qu, C. M. Fadzen, J. M. Wolfe, M. S. Regan, B. L. Pentelute, N. Y. R. Agar and C. F. Cho, *Nat Protoc*, 2018, **13**, 2827-2843.

75. T. E. Park, N. Mustafaoglu, A. Herland, R. Hasselkus, R. Mannix, E. A. FitzGerald, R. Prantil-Baun, A. Watters, O. Henry, M. Benz, H. Sanchez, H. J. McCrea, L. C. Goumnerova, H. W. Song, S. P. Palecek, E. Shusta and D. E. Ingber, *Nat Commun*, 2019, **10**, 2621.

76. D. R. Zimmermann and M. T. Dours-Zimmermann, *Histochem Cell Biol*, 2008, **130**, 635-653.

77. J. Arulmoli, H. J. Wright, D. T. T. Phan, U. Sheth, R. A. Que, G. A. Botten, M. Keating, E. L. Botvinick, M. M. Pathak, T. I. Zarembinski, D. S. Yanni, O. V. Razorenova, C. C. W. Hughes and L. A. Flanagan, *Acta Biomater*, 2016, **43**, 122-138.

78. A. L. Placone, P. M. McGuiggan, D. E. Bergles, H. Guerrero-Cazares, A. Quinones-Hinojosa and P. C. Searson, *Biomaterials*, 2015, **42**, 134-143.

79. A. F. Levy, M. Zayats, H. Guerrero-Cazares, A. Quinones-Hinojosa and P. C. Searson, *PLoS One*, 2014, **9**, e92165.

80. P. P. Partyka, G. A. Godsey, J. R. Galie, M. C. Kosciuk, N. K. Acharya, R. G. Nagele and P. A. Galie, *Biomaterials*, 2017, **115**, 30-39.

81. R. F. Haseloff, I. E. Blasig, H. C. Bauer and H. Bauer, *Cellular and Molecular Neurobiology*, 2005, **25**, 25-39.

82. G. Fricker and D. S. Miller, *Pharmacology*, 2004, **70**, 169-176.

83. K. Arai, G. Jin, D. Navaratna and E. H. Lo, *FEBS J*, 2009, **276**, 4644-4652.

84. S. Nag, J. L. Takahashi and D. W. Kilty, *J Neuropathol Exp Neurol*, 1997, **56**, 912-921.

85. Y. Fan and G. Y. Yang, *J Neuroimmune Pharmacol*, 2007, **2**, 284-289.

86. D. Barata, C. van Blitterswijk and P. Habibovic, *Acta Biomater*, 2016, **34**, 1-20.

87. D. Bumcrot, M. Manoharan, V. Koteliansky and D. W. Sah, *Nature chemical biology*, 2006, **2**, 711-719.

88.   A. Fire, S. Xu, M. K. Montgomery, S. A. Kostas, S. E. Driver and C. C. Mello, *nature*, 1998, **391**, 806-811.

89.   X. Xu, J. Wu, Y. Liu, P. E. Saw, W. Tao, M. Yu, H. Zope, M. Si, A. Victorious, J. Rasmussen, D. Ayyash, O. C. Farokhzad and J. Shi, *ACS Nano*, 2017, **11**, 2618-2627.

90.   J. Li, C. Wu, W. Wang, Y. He, E. Elkayam, L. Joshua-Tor and P. T. Hammond, *Proceedings of the National Academy of Sciences*, 2018, **115**, E2696.

91.   Y. Takei, K. Kadomatsu, Y. Yuzawa, S. Matsuo and T. Muramatsu, *Cancer research*, 2004, **64**, 3365-3370.

92.   F. Pittella, K. Miyata, Y. Maeda, T. Suma, S. Watanabe, Q. Chen, R. J. Christie, K. Osada, N. Nishiyama and K. Kataoka, *Journal of controlled release*, 2012, **161**, 868-874.

93.   G. Zheng, R. Zhao, A. Xu, Z. Shen, X. Chen and J. Shao, *European Journal of Pharmaceutical Sciences*, 2018, **111**, 492-502.

94.   W. J. Kim, L. V. Christensen, S. Jo, J. W. Yockman, J. H. Jeong, Y.-H. Kim and S. W. Kim, *Molecular Therapy*, 2006, **14**, 343-350.

95.   S. Kim, Y. Choi, G. Park, C. Won, Y.-J. Park, Y. Lee, B.-S. Kim and D.-H. Min, *Nano Research*, 2016, **10**, 503-519.

96.   A. Mukherjee, V. S. Madamsetty, M. K. Paul and S. Mukherjee, *Int J Mol Sci*, 2020, **21**.

97.   S. K. Nethi, A. K. Barui, S. Mukherjee and C. R. Patra, *Antioxid Redox Signal*, 2019, **30**, 786-809.

98.   S. Lee, J. Lim, J. Yu, J. Ahn, Y. Lee and N. L. Jeon, *Lab on a Chip*, 2019, **19**, 2071-2080.

99.   S. Lee, J. Ko, D. Park, S.-R. Lee, M. Chung, Y. Lee and N. L. Jeon, *Lab on a Chip*, 2018, **18**, 2686-2709.

100.   J. Ko, J. Ahn, S. Kim, Y. Lee, J. Lee, D. Park and N. L. Jeon, *Lab on a Chip*, 2019, **19**, 2822-2833.

101.   M. Chung, J. Ahn, K. Son, S. Kim and N. L. Jeon, *Advanced healthcare materials*, 2017, **6**, 1700196.

102.   Y. Nashimoto, R. Okada, S. Hanada, Y. Arima, K. Nishiyama, T. Miura and R. Yokokawa, *Biomaterials*, 2020, **229**, 119547.

103. C. Kim, J. Kasuya, J. Jeon, S. Chung and R. D. Kamm, *Lab on a chip*, 2015, **15**, 301-310.

104. J. Paek, S. E. Park, Q. Lu, K.-T. Park, M. Cho, J. M. Oh, K. W. Kwon, Y.-s. Yi, J. W. Song, H. I. Edelstein, J. Ishibashi, W. Yang, J. W. Myerson, R. Y. Kiseleva, P. Aprelev, E. D. Hood, D. Stambolian, P. Seale, V. R. Muzykantov and D. Huh, *ACS Nano*, 2019, **13**, 7627-7643.

105. P. Agarwal, H. Wang, M. Sun, J. Xu, S. Zhao, Z. Liu, K. J. Gooch, Y. Zhao, X. Lu and X. He, *ACS Nano*, 2017, **11**, 6691-6702.

106. H.-F. Wang, R. Ran, Y. Liu, Y. Hui, B. Zeng, D. Chen, D. A. Weitz and C.-X. Zhao, *ACS Nano*, 2018, **12**, 11600-11609.

107. J. Ahn, Y. J. Sei, N. L. Jeon and Y. Kim, *IEEE Transactions on Nanotechnology*, 2017, **17**, 393-397.

108. N. J. Halas, *ACS nano*, 2008, **2**, 179-183.

109. E. P. o. F. Additives, N. S. a. t. Food, M. Younes, P. Aggett, F. Aguilar, R. Crebelli, B. Dusemund, M. Filipič, M. J. Frutos, P. Galtier and D. Gott, *EFSA Journal*, 2018, **16**, e05088.

110. R. R. Castillo, D. Lozano and M. Vallet-Regí, *Pharmaceutics*, 2020, **12**, 432.

111. S. Kim, H.-K. Na, C. Won and D.-H. Min, *RSC advances*, 2016, **6**, 27143-27150.

112. H.-K. Na, M.-H. Kim, K. Park, S.-R. Ryoo, K. E. Lee, H. Jeon, R. Ryoo, C. Hyeon and D.-H. Min, *Small*, 2012, **8**, 1752-1761.

113. S. Y. Lee, C. Y. Yang, C. L. Peng, M. F. Wei, K. C. Chen, C. J. Yao and M. J. Shieh, *Biomaterials*, 2016, **86**, 92-105.

114. L. Espana-Serrano and M. B. Chougule, *Molecular Therapy-Nucleic Acids*, 2016, **5**, e384.

115. B. G. Coon, N. Baeyens, J. Han, M. Budatha, T. D. Ross, J. S. Fang, S. Yun, J. L. Thomas and M. A. Schwartz, *J Cell Biol*, 2015, **208**, 975-986.

116. T. Issitt, E. Bosseboeuf, N. De Winter, N. Dufton, G. Gestri, V. Senatore, A. Chikh, A. M. Randi and C. Raimondi, *iScience*, 2019, **11**, 205-223.

117. G. Haqshenas, J. Wu, K. J. Simpson, R. J. Daly, H. J. Netter, T. F. Baumert and C. Doerig, *Nat Commun*, 2017, **8**, 15158.

118. T. Saito, N. Takeda, E. Amiya, T. Nakao, H. Abe, H. Semba, K. Soma, K. Koyama, Y. Hosoya, Y. Imai, T. Isagawa, M. Watanabe, I. Manabe, I. Komuro, R. Nagai and K. Maemura, *FEBS Lett*, 2013, **587**, 2179-2185.

119. E. Zudaire, L. Gambardella, C. Kurcz and S. Vermeren, *PloS one*, 2011, **6**, e27385.

120. F. Danhier, O. Feron and V. Préat, *Journal of controlled release*, 2010, **148**, 135-146.

121. J. Ahn, J. Ko, S. Lee, J. Yu, Y. Kim and N. L. Jeon, *Advanced drug delivery reviews*, 2018, **128**, 29-53.

122. A. Eberhard, S. Kahlert, V. Goede, B. Hemmerlein, K. H. Plate and H. G. Augustin, *Cancer research*, 2000, **60**, 1388-1393.

123. Y. D. Jung, S. A. Ahmad, Y. Akagi, Y. Takahashi, W. Liu, N. Reinmuth, R. M. Shaheen, F. Fan and L. M. Ellis, *Cancer and Metastasis Reviews*, 2000, **19**, 147-157.

124. M. Alevizakos, S. Kaltsas and K. N. Syrigos, *Cancer chemotherapy and pharmacology*, 2013, **72**, 1169-1181.

125. H.-C. Sun and Z.-Y. Tang, *Journal of cancer research and clinical oncology*, 2004, **130**, 307-319.

126. D. Huh, B. D. Matthews, A. Mammoto, M. Montoya-Zavala, H. Y. Hsin and D. E. Ingber, *Science*, 2010, **328**, 1662-1668.

127. N. Korin, M. Kanapathipillai, B. D. Matthews, M. Crescente, A. Brill, T. Mammoto, K. Ghosh, S. Jurek, S. A. Bencherif and D. Bhatta, *Science*, 2012, **337**, 738-742.

128. A. Herland, A. D. van der Meer, E. A. FitzGerald, T.-E. Park, J. J. Sleeboom and D. E. Ingber, *PLoS One*, 2016, **11**, e0150360.

129. B. A. Hassell, G. Goyal, E. Lee, A. Sontheimer-Phelps, O. Levy, C. S. Chen and D. E. Ingber, *Cell reports*, 2017, **21**, 508-516.

130. T.-E. Park, N. Mustafaoglu, A. Herland, R. Hasselkus, R. Mannix, E. A. FitzGerald, R. Prantil-Baun, A. Watters, O. Henry and M. Benz, *Nature communications*, 2019, **10**, 1-12.

131. A. Sobrino, D. T. Phan, R. Datta, X. Wang, S. J. Hachey, M. Romero-Lopez, E. Gratton, A. P. Lee, S. C. George and C. C. Hughes, *Sci Rep*, 2016, **6**, 31589.

132. D. T. T. Phan, X. Wang, B. M. Craver, A. Sobrino, D. Zhao, J. C.

Chen, L. Y. N. Lee, S. C. George, A. P. Lee and C. C. W. Hughes, *Lab Chip*, 2017, **17**, 511-520.

133. T. Osaki, J. C. Serrano and R. D. Kamm, *Regen Eng Transl Med*, 2018, **4**, 120-132.

134. K. Haase, G. S. Offeddu, M. R. Gillrie and R. D. Kamm, *Advanced Functional Materials*, 2020, DOI: 10.1002/adfm.202002444.

135. V. Vickerman and R. D. Kamm, *Integrative Biology*, 2012, **4**, 863-874.

136. S. Lee, M. Chung, S. R. Lee and N. L. Jeon, *Biotechnology and Bioengineering*, 2020, **117**, 748-762.

137. S. K. Hobbs, W. L. Monsky, F. Yuan, W. G. Roberts, L. Griffith, V. P. Torchilin and R. K. Jain, *Proceedings of the National Academy of Sciences*, 1998, **95**, 4607-4612.

138. A. C. Newman, M. N. Nakatsu, W. Chou, P. D. Gershon and C. C. Hughes, *Molecular biology of the cell*, 2011, **22**, 3791-3800.

139. E. Van Cutsem, C.-H. Köhne, E. Hitre, J. Zaluski, C.-R. Chang Chien, A. Makhson, G. D'haens, T. Pintér, R. Lim and G. Bodoky, *New England Journal of Medicine*, 2009, **360**, 1408-1417.

140. E. C. Gamelin, E. M. Danquechin-Dorval, Y. F. Dumesnil, P. J. Maillart, M. Goudier, P. C. Burtin, R. G. Delva, A. H. Lortholary, P. H. Gesta and F. G. Larra, *Cancer: Interdisciplinary International Journal of the American Cancer Society*, 1996, **77**, 441-451.

141. D. B. Longley, D. P. Harkin and P. G. Johnston, *Nature reviews cancer*, 2003, **3**, 330.

142. R. J. Kelly and O. Rixe, *Targeted oncology*, 2009, **4**, 297-305.

143. P. Garcia-Alfonso, E. Grande, E. Polo, R. Afonso, J. J. Reina, M. Jorge, J. M. Campos, V. Martinez, C. Angeles and C. Montagut, *Angiogenesis*, 2014, **17**, 805-821.

144. D. Cunningham, Y. Humblet, S. Siena, D. Khayat, H. Bleiberg, A. Santoro, D. Bets, M. Mueser, A. Harstrick and C. Verslype, *New England journal of medicine*, 2004, **351**, 337-345.

145. D. J. Jonker, C. J. O'callaghan, C. S. Karapetis, J. R. Zalcberg, D. Tu, H.-J. Au, S. R. Berry, M. Krahn, T. Price and R. J. Simes,

New England Journal of Medicine, 2007, **357**, 2040-2048.

146. A. Lievre, J.-B. Bachet, D. Le Corre, V. Boige, B. Landi, J.-F. Emile, J.-F. Côté, G. Tomasic, C. Penna and M. Ducreux, *Cancer research*, 2006, **66**, 3992-3995.

147. J. Lee, I. Lee, B. Han, J. O. Park, J. Jang, C. Park and W. K. Kang, *JNCI: Journal of the National Cancer Institute*, 2011, **103**, 674-688.

148. S. S. Kumar, T. J. Price, O. Mohyieldin, M. Borg, A. Townsend and J. E. Hardingham, *Gastrointestinal cancer research: GCR*, 2014, **7**, 23.

149. G. Fricker and D. S. Miller, *Pharmacology*, 2004, **70**, 169-176.

150. M. Vallon, J. Chang, H. Zhang and C. J. Kuo, *Cellular and molecular life sciences*, 2014, **71**, 3489-3506.

151. Y. Fan and G.-Y. Yang, *Journal of Neuroimmune Pharmacology*, 2007, **2**, 284-289.

152. K. Arai, G. Jin, D. Navaratna and E. H. Lo, *The FEBS journal*, 2009, **276**, 4644-4652.

153. D. Barata, C. van Blitterswijk and P. Habibovic, *Acta biomaterialia*, 2016, **34**, 1-20.

154. S. Lee, S. Kim, D.-J. Koo, J. Yu, H. Cho, H. Lee, J. M. Song, S.-Y. Kim, D.-H. Min and N. L. Jeon, *ACS nano*, 2020.

155. S. Lee, H. Kang, D. Park, J. Yu, S. K. Koh, D. Cho, D. H. Kim, K. S. Kang and N. L. Jeon, *Advanced Biology*, 2000195.

국문 초록

혈관 신생은 혈관망의 장기 특이적인 기능을 부여하게
하는 중요한 과정임과 동시에, 여러 질병 및 병변에서 흔히 발
견되는 현상이다. 또한 암 혈관 신생은 암을 판단하는 중요한
지표 역할을 하기도 하며, 현재 암 치료제의 대부분은 혈관 신
생을 조절하는 기작을 기반으로 한다. 이와 같이 다양한 생리
학적, 병리학적 의미를 가지는 혈관 신생 연구는 활발하게 진
행되고 있지만 연구에 사용되는 모델들은 여러 방면에서 한계
를 지닌다. 특히 체내 모델의 경우 다양한 타겟의 약물 후보군
을 테스트할 수 있는 효율성이 낮고, 이차원 체외 모델의 경우
복잡한 삼차원 혈관 신생을 제대로 반영하지 못하고 있다. 이
를 극복하기 위해 미세유체 기반의 삼차원 체외 공배양 모델
이 도입되고 있다. 본 박사학위심사 논문에서는 다양한 전임상
연구에 활용될 수 있는 혈관 생 모델을 소개하고자 한다.

우선 혈관망의 장기 특이적 기능을 모사하기 위해 혈관 신
생 모델을 도입하였다. 인간의 뇌에는 장벽 기능을 하는 혈액-
뇌 장벽으로 불리는 혈관망이 존재한다. 이 혈관망은 발달 과
정에서 혈관 신생 기작을 기반으로 그 장벽 기능을 발달시키
기 때문에, 본 연구에서는 혈관 신생을 통해 장벽 기능에 기여
하는 주변 세포들과 혈관의 상호작용을 더 증진시키는 결과를
얻었다. 또한 다양한 장벽 기능 중 Efflux Transport System이 본
모델에서 구현된 것을 확인하였고, 그 저해제를 처리하였을 때

혈액-뇌 장벽 모델에서 더 효과적으로 Efflux Transport 기능이 저해되는 것을 확인하였다. 이런 혈관 신생을 기반으로 한 모델은 기능적인 체외 모델 개발을 가능하게 하여 추후 본 모델을 활용한 질병의 연구 및 약물의 효능 평가에서 더 신뢰성 있는 결과를 도출할 수 있을 것으로 기대한다.

또 다른 전임상 연구로는 다양한 항암제를 시험할 수 있는 암 혈관 신생 모델을 개발하였다. 특히 항암제 중 유전자 치료제의 효능 평가가 효율적이고 효과적으로 이루어지지 않고 있다는 기존 연구들의 한계를 극복하기 위해, 삼차원 암 혈관 신생 모델이 도입되었다. 삼차원 혈관 신생 모델을 통해 이차원 혈관 세포 배양에서는 확인하기 힘들었던 타겟 유전자에 따른 약의 효능 차이를 검증할 수 있었다. 또한 다양한 암 종류 중에 약물의 효능이 제일 좋은 암 종류를 효율적으로 선별할 수 있었다. 이런 연구 결과는 기존의 체외 모델에서는 볼 수 없었던 삼차원 혈관 신생의 특징들에 대한 관찰을 가능하게 할뿐더러, 체내 모델 혹은 임상에서의 더 구체화된 관찰을 진행하기 전 약물의 타겟 범위를 효율적으로 좁혀 나갈 수 있는 기회를 제공한다. 추가적으로 플라스틱 칩을 기반으로 한 암 혈관 모델을 소개하였는데, 이는 해당 체외 모델이 추후 고효율 대용량 약물 스크리닝에 이용될 수 있는 가능성을 보여준다.

이와 같이 삼차원 혈관 신생을 이용한 질병 연구 및 치료제의 스크리닝은 치료제 개발을 위한 전임상 과정에서의 비용과 부정확한 결과를 최소화하고 임상 과정 전까지의 과정의 정확성과 효율성을 극대화할 것으로 기대한다.